SARS-CoV-2 Spike triggers barrier dysfunction and vascular leak via integrins and TGF-β signaling

Scott B. Biering[1][*][†], Francielle Tramontini Gomes de Sousa[1][*], Laurentia V. Tjang[1], Felix Pahmeier[1], Richard Ruan[1], Sophie F. Blanc[1], Trishna S. Patel[1], Caroline M. Worthington[2], Dustin R. Glasner[3,4], Bryan Castillo-Rojas[1], Venice Servellita[3,4], Nicholas T.N. Lo[1], Marcus P. Wong[1], Colin M. Warnes[1], Daniel R. Sandoval[5], Thomas Mandel Clausen[5], Yale A. Santos[3,4], Victoria Ortega[6], Hector C. Aguilar[6], Jeffrey D. Esko[5], Charles Y. Chui[3,4,7,8], John E. Pak[2], P. Robert Beatty[1], Eva Harris[1,9][†]

[1]Division of Infectious Diseases and Vaccinology, School of Public Health, University of California, Berkeley, Berkeley, CA, USA

[2]Chan Zuckerberg Biohub, San Francisco, CA, USA

[3]Department of Laboratory Medicine, University of California, San Francisco, CA, USA

[4]UCSF-Abbott Viral Diagnostics and Discovery Center, San Francisco, CA, USA

[5]Department of Cellular and Molecular Medicine, Glycobiology Research and Training Center, University of California, San Diego, La Jolla, CA, USA

[6]Department of Microbiology and Immunology, Cornell University, Ithaca, NY, USA

[7]Innovative Genomics Institute, University of California, Berkeley, CA, USA

[8]Department of Medicine, University of California, San Francisco, CA, USA

[9]Lead contact

*These authors contributed equally to this work

†Correspondence: sbiering@berkeley.edu (S.B.B.), eharris@berkeley.edu (E.H.)

Summary

Severe COVID-19 is associated with epithelial and endothelial barrier dysfunction within the lung as well as in distal organs. While it is appreciated that an exaggerated inflammatory response is associated with barrier dysfunction, the triggers of this pathology are unclear. Here, we report that cell-intrinsic interactions between the Spike (S) glycoprotein of SARS-CoV-2 and epithelial/endothelial cells are sufficient to trigger barrier dysfunction *in vitro* and vascular leak *in vivo*, independently of viral replication and the ACE2 receptor. We identify an S-triggered transcriptional response associated with extracellular matrix reorganization and TGF-β signaling. Using genetic knockouts and specific inhibitors, we demonstrate that glycosaminoglycans, integrins, and the TGF-β signaling axis are required for S-mediated barrier dysfunction. Our findings suggest that S interactions with barrier cells are a contributing factor to COVID-19 disease severity and offer mechanistic insight into SARS-CoV-2 triggered vascular leak, providing a starting point for development of therapies targeting COVID-19 pathogenesis.

Introduction

Severe acute respiratory syndrome coronavirus-2 (SARS-CoV-2) is an emerging human pathogen belonging to the *Coronaviridae* family and the causative agent of coronavirus disease 2019 (COVID-19). Outcomes of SARS-CoV-2 infection range from asymptomatic to non-severe COVID-19 with flu-like symptoms that can progress to severe cases associated with acute lung injury and acute respiratory distress syndrome (ARDS) (1-3). The lung pathology of severe COVID-19 involves pulmonary edema stemming from endothelial and epithelial barrier dysfunction believed to be induced by an exacerbated inflammatory response (4-6); however, the specific triggers of this inflammatory response and the involvement of particular viral factors in this pathology are not completely understood.

SARS-CoV-2 possesses a ~30-kb positive-sense RNA genome encoding for ~29 proteins including four structural proteins: spike (S), nucleocapsid (N), matrix (M), and envelope (E) (7, 8). Homotrimers of the S glycoprotein coat the SARS-CoV-2 virion and engage the viral receptor, angiotensin converting enzyme 2 (ACE2), on the surface of susceptible cells to mediate viral entry (9, 10). S consists of two subunits, S1 -- containing the receptor-binding domain (RBD) that engages ACE2, and S2 -- containing the fusion machinery required for virus-cell membrane fusion (7, 11, 12). Two cleavage sites, S1/S2 and S2' separate S1 and S2 and must be cleaved by host proteases for S to mediate virus-cell fusion. Furin-like proteases, cathepsin L, and TMPRSS2 are able to cleave these sites, making them essential host factors for SARS-CoV-2 infection (10, 13-15). RBD engagement of ACE2 triggers conformational changes in S that result in S1 shedding and insertion of the fusion peptide into the host membrane (16, 17).

In addition to ACE2, the SARS-CoV-2 S glycoprotein has been reported to engage numerous cell-surface host factors, including heparan sulfate-containing proteoglycans (HSPG) and integrins, which are proposed to serve as attachment factors promoting SARS-CoV-2 entry (18-20). Beyond facilitating viral entry, the engagement of S with these host factors may mediate signaling pathways contributing to lung pathology. Indeed, it was demonstrated that engagement of ACE2 by SARS-CoV-1 S results in depletion of ACE2 from the cell surface, leading to an imbalance in the renin-angiotensin system and thus promoting inflammatory responses, barrier dysfunction, and lung injury (21-23). A comparable ACE2-dependent pathway has been described for SARS-CoV-2 S (24-26). A unique element of the SARS-CoV-2 entry cascade is that the RBD-containing S1 portion of S can be shed from the surface of virions following engagement of the ACE2 receptor, suggesting that shed-S1 may also promote pathology via interactions with epithelial and endothelial cells independently of the virion (16, 17). While interactions between the SARS-CoV-2 S glycoprotein and the cell surface may promote pathology such as barrier dysfunction, the mechanisms by which this occurs and the host factors involved are not well understood.

We and others have recently described a phenomenon by which viral proteins, such as the flavivirus non-structural protein 1 (NS1), interact with endothelial cells to trigger signaling cascades that mediate disruption of cellular structures required for endothelial barrier integrity, including the endothelial glycocalyx layer (EGL) and intercellular junctional complexes (27-32). This has led to the designation of flavivirus NS1 protein as a "viral toxin" that can mediate barrier dysfunction and promote viral dissemination and pathogenesis (33). Here, we investigated this possibility for SARS-CoV-2 S by studying the contribution of S to endothelial and epithelial barrier dysfunction *in vitro* and vascular leak *in vivo.* Our study revealed that full-length S and the RBD from SARS-CoV-2 were sufficient to mediate barrier dysfunction and vascular leak in an ACE2-

independent manner. Further, transcriptional analyses showed that S modulates expression of transcripts involved in regulation of the extracellular matrix (ECM), revealing a mechanism in which glycosaminoglycans (GAGs), integrins, and transforming growth factor beta (TGF-β) signaling are required for barrier dysfunction. These data uncover the role of SARS-CoV-2 S in promoting barrier dysfunction and provide critical mechanistic insight into COVID-19 pathogenesis, highlighting new avenues for therapeutic intervention.

Results

SARS-CoV-2 S mediates endothelial and epithelial hyperpermeability

To determine whether SARS-CoV-2 S can mediate barrier dysfunction independently from SARS-CoV-2 infection, we initially utilized a trans-epithelial/endothelial electrical resistance (TEER) assay. Using TEER, we measured the electrical resistance across a monolayer of human pulmonary microvascular endothelial cells (HPMEC) or human lung epithelial cells (Calu-3) seeded in the apical chamber of transwells as a proxy of barrier permeability **(Figure 1A)**. We selected HPMEC as a representative endothelial cell because of the lung pathology associated with COVID-19 and because they do not endogenously express ACE2 and are not permissive to SARS-CoV-2 infection, thus allowing us to separate viral infection from S-mediated barrier dysfunction **(Figures S1A and S1B)**. We produced recombinant soluble trimeric S and RBD in-house for experiments, which we determined were of high purity **(Figures S1C-E)**.

Parental HPMEC were treated with soluble trimeric SARS-CoV-2 S, as well as dengue virus (DENV) NS1 and vascular endothelial growth factor (VEGF) as positive controls. As seen previously, treatment of HPMEC with DENV NS1 led to a reversible decrease in barrier resistance that peaked around 6 hours post-treatment (hpt) **(Figure 1B)**. Interestingly, SARS-CoV-2 S also triggered a reversible barrier dysfunction in parental HPMEC but with distinct temporal kinetics, reaching a peak ~24 hpt. Since HPMEC do not endogenously express ACE2, these data suggest that S triggers barrier dysfunction in a manner independently of ACE2 **(Figure 1B)**. Given that S-triggered endothelial hyperpermeability peaked at 24 hpt, we utilized this timepoint for subsequent experiments. We next treated both parental HPMEC or HPMEC overexpressing human ACE2 (HPMEC/ACE2) with soluble trimeric SARS-CoV-2 S and found that S triggered endothelial hyperpermeability in a dose-dependent manner **(Figure 1C)**. We found that S triggered barrier dysfunction comparably in both parental HPMEC and HPMEC/ACE2, further suggesting that this phenotype is independent of ACE2 **(Figure 1C)**. To determine whether virion-bound S was also able to trigger endothelial hyperpermeability, we utilized vesicular stomatitis virus (VSV) pseudotyped with SARS-CoV-2 S (VSV-S), along with VSV expressing VSV glycoprotein (VSV-G) or no glycoprotein (VSV-bald) as negative controls. Comparable to soluble S and the VEGF positive control, VSV-S also triggered endothelial hyperpermeability in a dose-dependent manner, whereas VSV-G and VSV-bald had no effect on barrier function. Again, no significant differences were observed in relative TEER values when comparing results for HPMECs and HPMEC/ACE2 **(Figure 1D)**. Further, we found that recombinant SARS-CoV-2 S RBD was sufficient to trigger a drop in TEER in HPMEC in a dose-dependent manner **(Figure 1E)**. We next tested the capacity of S to trigger epithelial hyperpermeability of Calu-3 cells in a TEER assay and found that full-length trimeric S and the RBD were indeed sufficient to trigger epithelial hyperpermeability **(Figure 1F)**. To confirm that the phenotype was specific to S, we measured the ability of anti-S antibodies to inhibit S-induced barrier dysfunction and found that a cocktail of two anti-S

antibodies abolished S-mediated endothelial hyperpermeability **(Figure 1G)**. Taken together, these data indicate that SARS-CoV-2 S and its RBD can facilitate barrier hyperpermeability in both human lung endothelial and epithelial cells.

SARS-CoV-2 S triggers disruption of the endothelial and epithelial glycocalyx layer

Cell surface proteins on epithelial and endothelial surfaces are surrounded by a dense mesh of glycans termed the epithelial/endothelial glycocalyx layer (EGL). The EGL includes sialic acid and glycosaminoglycans (GAGs) and serves as a critical determinant of barrier function, protecting epithelial and endothelial cells from shear stress (34). Previous work has demonstrated that flavivirus NS1 glycoproteins mediate endothelial dysfunction through disruption of the EGL via activation of EGL-degrading enzymes (28, 30). To determine if SARS-CoV-2 S disrupts the EGL, we treated HPMEC and Calu-3 cells with S and measured the surface levels of key EGL components, including sialic acid (SIA), heparan sulfate (HS), hyaluronic acid (HA), and chondroitin sulfate (CS) by immunofluorescence assay (IFA). We also measured the levels of hyaluronidase and neuraminidase, which degrade hyaluronan and sialylated glycans, respectively. We found that S treatment of both HPMEC and Calu-3 cells resulted in a significant decrease in EGL components compared to control conditions, and conversely, led to upregulation of EGL-degrading enzymes **(Figures 2A-H)**. These data suggest that, like flavivirus NS1, SARS-CoV-2 S mediates disruption of the EGL.

Although our parental HPMEC are not permissive to SARS-CoV-2 infection and had no detectable levels of ACE2 as determined by western blot, we utilized CRISPR-CAS9 to introduce double-stranded breaks in the ACE2 gene to rule out the possibility that low levels of ACE2 present on the cell surface could be contributing to our phenotype. We found that S-mediated EGL disruption was comparable in HPMECs transduced with lentivirus encoding ACE2-targeting guide RNAs or non-targeting guides (NT), further supporting that SARS-CoV-2 S-triggered barrier dysfunction can occur independently of ACE2 **(Figures S1F and S1G)**. Finally, we tested whether S from multiple SARS-CoV-2 variants of concern could trigger barrier dysfunction and found that, comparable to S protein from the ancestral Wuhan variant, S derived from alpha, beta, gamma, and delta variants could all facilitate EGL disruption of HPMEC, indicating that this phenomenon is not specific to one variant, but instead is a generalizable property of SARS-CoV-2 S **(Figures S1H and S1I)**.

SARS-CoV-2 S triggers vascular leak *in vivo*

To determine whether SARS-CoV-2 S could mediate vascular leak *in vivo*, we utilized our previously characterized dermal leak model, which involves local intradermal injection of compounds into distinct spots in the dorsal dermis of mice followed by intravenous administration of dextran conjugated to Alexa fluor 680 to serve as a tracer. Following a 2-hour incubation, mice were euthanized and the local relative accumulation of dextran-680 in the dorsal dermis was measured by a fluorescent scanner (29, 31, 35). Given our observations that SARS-CoV-2 S mediates barrier dysfunction in an ACE2-independent manner, we utilized WT C57BL/6J mice that do not express human ACE2 and are not permissive to infection by most SARS-CoV-2 variants including the Wuhan and Washington isolates (9, 36). We observed that, comparably to the DENV NS1 positive control, SARS-CoV-2 S induced vascular leak in the dorsal dermis of mice above control conditions, indicating that SARS-CoV-2 S is sufficient to trigger vascular leak *in vivo* **(Figures 3A and 3B)**. To test if SARS-CoV-2 S could mediate vascular leak when administered in a more physiologically relevant route, we administered S intranasally and then

5

measured accumulation of dextran-680 in various organs to evaluate both local (lungs) and distal (spleen, small intestine, liver, and brain) vascular leak. We found that SARS-CoV-2 S significantly induced vascular leak locally in the lungs as well as distally in the spleen and small intestine, with trending but non-significant leak measured in the liver and brain, as determined through accumulation of dextran-680 **(Figures 3C-H and Figures S2A-D)**.

Glycosaminoglycans are required for S-mediated barrier dysfunction

Given that S interactions with HSPGs enhance infectivity of SARS-CoV-2 (20, 37), we hypothesized that cell surface GAGs are also required for S-mediated barrier dysfunction. We measured the capacity of heparin, a highly charged linear polysaccharide analogous to heparan sulfate, to antagonize S-mediated endothelial hyperpermeability and found that heparin decreased S-induced endothelial hyperpermeability in a TEER assay, supporting our hypothesis that interactions with sulfated glycans on the cell surface contribute to S-mediated barrier dysfunction **(Figure 4A)**. To further test the contributions of glycans to S-mediated barrier dysfunction, we utilized recombinant enzymes to remove specific glycans from the surface of endothelial cells, including HS (heparin lyases), HA (hyaluronidase), CS (chondroitinase), or sialic acid (neuraminidase) and tested the ability of S to trigger barrier dysfunction under each of these conditions. We found that removal of HS, HA, or CS, but not sialic acid, inhibited S-mediated endothelial hyperpermeability, further supporting a role for GAGs in S-mediated barrier dysfunction **(Figures 4B and S3A)** as measured by TEER. Removal of HS and HA was also sufficient to abrogate S-mediated EGL disruption **(Figure 4C and 4D)**. To genetically investigate the contribution of HS to this phenotype, we utilized CRISPR-Cas9 technology to produce cell lines with two genes individually knocked out that are involved in the HS proteoglycan biosynthetic pathway; namely, SLC35B2 and XYLT2 (37-40). We confirmed that these KO cell lines possessed less detectable HS on the cell surface as compared to the NT controls **(Figure S3B and S3C)**. When we treated these cell lines with S, we found that they were less susceptible to S-mediated barrier dysfunction compared to the NT controls, providing further evidence of the involvement of GAGs in this pathway **(Figure 4E and 4F)**.

Extracellular matrix modulating-components contribute to SARS-CoV-2 S-mediated barrier dysfunction

We next hypothesized that components reported to be critical for flavivirus NS1-mediated EGL disruption may contribute to S-mediated EGL disruption. Therefore, we investigated the involvement of several endogenous enzymes and factors known to regulate the homeostasis of the ECM, including cathepsin L, heparanase (HPSE), A Disintegrin And Metalloprotease 17 (ADAM17), IL-6R, and matrix metalloproteinase 9 (MMP9). Cathepsin L, HPSE, and MMP9 are known to be critical for flavivirus NS1-mediated endothelial barrier dysfunction (28, 29, 41, 42). MMP9 is reported to be involved in release of the ECM-modulating TGF-β (43). ADAM17 has been implicated in modulation of COVID-19 pathogenesis through regulation of ACE2 shedding, IL6 signaling, and TGF-β signaling (44, 45). We produced KO HPMEC for each of these factors and found that HPMECs genetically deficient in HPSE, ADAM17, and MMP9 were no longer sensitive to S-mediated barrier dysfunction. In contrast, HPMEC deficient for cathepsin L and IL6R displayed comparable barrier dysfunction to NT control HPMEC **(Figures 4G and S3D-H)**. These data highlight the requirement of critical modulators of the EGL for S-mediated barrier dysfunction and further reveal differences by which S and flavivirus NS1 mediate barrier dysfunction.

Transcriptional analysis reveals SARS-CoV-2 S modulation of genes involved in extracellular matrix homeostasis

To gain further insight into the effects of S on endothelial cells, we conducted RNA sequencing (RNA-seq) to measure the global transcriptional profile of HPMEC and HPMEC/ACE2 following treatment with S. In S-treated HPMEC, we identified 65 differentially expressed genes (DEGs) compared to untreated controls, including 45 upregulated and 20 downregulated genes; in S-treated HPMEC/ACE2, there were 42 DEGs, with 34 upregulated and 7 downregulated compared to untreated controls. Further, the DEGs obtained from HPMEC and HPMEC/ACE2 were similar, indicating ACE2 expression has minimal impact on the HPMEC transcriptional response to S. **(Figures 5A, 5B, S4A, and S4B, Table S1, and S2)**. We observed numerous genes encoding ECM components, including proteoglycans, collagens and integrins, as well as genes coding for proteins involved in ECM degradation, such as CAPN2 (calpain), an endothelial cysteine protease, and HTRA1, which is responsible for degradation of fibronectin and proteoglycans, in agreement with our observations that S disrupts the EGL (46). Upregulation of XYLT2 (xylosyltransferase 2), an enzyme responsible for biosynthesis of CS, HS, and dermatan sulfate proteoglycans, is potentially involved in an EGL recovery pathway, post-S-mediated barrier dysfunction. Transcriptome profiling also showed activation of the TGFβ signaling pathway, demonstrated by upregulation of TGFBI, LTBP2, LTBP3, SERPINE1, FBLN5, POSTN, FN1, THBS1, BGN, ITGB5, and ITGA4 genes. TGF-β is a well-known mediator of cellular differentiation, proliferation, and migration, with an important role in the regulation of vascular permeability and inflammatory responses (47). We next conducted a protein-protein interaction network analysis of upregulated genes from parental HPMEC to examine the relationships between these DEGs. We found that S-upregulated genes form a highly interconnected matrix with predicted protein interactions, pinpointing 31 genes of ECM or ECM-associated proteins, including numerous components of the focal adhesion complex that connects the cytoskeleton of barrier cells to the ECM via integrins (48) **(Figure 5C)**. Given these observations, we hypothesized that S-mediated barrier dysfunction requires integrins, which in turn promote TGF-β maturation and signaling.

Integrins are required for S-mediated barrier dysfunction

Integrins are transmembrane proteins that are critical for maintaining barrier function by connecting cells to the ECM (49). Integrins interact with factors regulating ECM homeostasis, such as the latency associated peptide (LAP), which non-covalently binds to TGF-β, maintaining it in an inactive form (50). LAP releases the active form of TGF-β in response to diverse stimuli, including mechanical stress, or through competition with integrin-binding factors (resulting in the release of LAP from the ECM) (50). Integrins mediate these interactions via a small peptide motif (RGD) on interacting proteins (50, 51). Recombinant RGD peptides are commonly used as integrin-binding motifs that can compete for integrin binding with other RGD-containing proteins like LAP and TGF-β (52). Further, it has been reported that SARS-CoV-2 S has evolved an RGD motif within its RBD (19). However, although SARS-CoV-2 S has been shown to bind to integrins, the functional relevance of this motif is unclear (18). To test for a role of integrins in S-mediated barrier dysfunction, we measured the capacity of an integrin inhibitor (ATN-161) to inhibit S-mediated hyperpermeability in both a TEER assay and an EGL disruption assay. We found that ATN-161 treatment of cells abrogated S-mediated barrier dysfunction relative to control conditions in a dose-dependent manner, while having no effect on barrier function alone **(Figures 6A, 6B, S5A, and S5B)**. The dependence of S-mediated barrier dysfunction on integrins was independent of ACE2 expression, as S-mediated TEER drop was equivalently abrogated by ATN-161 in both HPMEC and HPMEC/ACE2 cells **(Figure 6A)**. To confirm the role of integrins in S-mediated

7

vascular leak *in vivo*, we tested the capacity of ATN-161 to inhibit leak in the intradermal leak model. We found that ATN-161 significantly inhibited S-mediated vascular leak while not mediating leak by itself, relative to a PBS control **(Figures 6C and 6D)**. We next tested whether a recombinant RGD peptide, mimicking the RGD motif within the SARS-CoV-2 S RBD, was sufficient to mediate endothelial hyperpermeability and EGL disruption in HPMEC. We utilized a KGD peptide (mimicking the corresponding sequence in SARS-CoV-1 S) as well as a DRG scrambled peptide as negative controls. Intriguingly, we found that RGD was sufficient to trigger endothelial hyperpermeability and EGL disruption comparably to S, whereas the effect of KGD and DRG on barrier function was comparable to the untreated control conditions **(Figures 6E, 6F, and S5C)**. Next, we tested the ability of the RGD peptide to trigger vascular leak *in vivo* in the intradermal leak model and found that, in agreement with the corresponding *in vitro* data, the RGD peptide was sufficient to trigger vascular leak in a dose-dependent manner and at comparable levels to full-length S **(Figures 6G and 6H)**. To genetically confirm a role for integrins, we used CRISPR-Cas9 to KO two RGD-binding integrins shown to interact with S, integrin alpha-5 (α5) and integrin beta-1 (β1) **(Figure 6I)**. We found that S-mediated barrier dysfunction was significantly inhibited in both KO HPMEC lines relative to the NT control HPMEC, with the caveat that relative barrier function was lower, compared to NT controls, in ITGA5 KO HPMECS **(Figures 6J, 6K, and SD)**. Taken together, these data indicate that integrins play a critical role in S-mediated barrier dysfunction and that the RGD of SARS-CoV-2 is an active motif contributing to pathology.

TGF-β signaling is essential for SARS-CoV-2 S-mediated barrier dysfunction

Integrins are key regulators of TGF-β maturation and signaling (47, 53). Given the critical role of integrins for SARS-CoV-2 S-mediated barrier dysfunction as well as our RNA-Seq data revealing S-mediated TGF-β transcriptional upregulation, we hypothesized that the RGD motif of SARS-CoV-2 S engages integrins, releasing mature TGF-β, which in turn activates signaling via interactions with the TGF-β receptor (TGFBR) and results in barrier dysfunction. To test this hypothesis, we measured levels of TGF-β in the supernatant of HPMECs treated with S and observed a significant increase in TGF-β in supernatants of S-treated cells compared to untreated control conditions **(Figure 7A)**. To determine the functional consequence of this TGF-β production, we treated HPMECs with recombinant TGF-β and found that this was sufficient to trigger endothelial hyperpermeability **(Figure 7B)**. To determine the contribution of TGF-β signaling to S-mediated endothelial dysfunction, we antagonized TGF-β signaling via antibody blockade of TGFBR1 and found that cells treated with anti-TGFBR1 were less sensitive to S-mediated endothelial hyperpermeability compared to control IgG conditions **(Figures 7C and S6A)**. Importantly, the anti-TGFBR1 antibody did not trigger endothelial hyperpermeability on its own **(Figure S6A)**. We next utilized a small-molecule inhibitor of TGF-β signaling (SB431542) and found that cells treated with this molecule were less responsive to S-mediated TEER drop and EGL disruption compared to the vehicle control-treated cells **(Figures 7D, 7E and S6C)**. Finally, we utilized CRISPR-Cas9 to produce TGFBR1 KO HPMECs **(Figure 7F)**. We found that these KO cells were less sensitive to S-mediated barrier dysfunction relative to the NT control cells **(Figures 7G, 7H, and S6D)**. Taken together, these data demonstrate that SARS-CoV-2 S triggers enhanced release of TGF-β from HPMEC and highlight a critical role for TGF-β signaling in S-mediated barrier dysfunction.

Discussion

Our study reveals the capacity and mechanism by which SARS-CoV-2 S mediates barrier dysfunction in epithelial and endothelial cells *in vitro* and vascular leak *in vivo*, thus suggesting that S alone can mediate barrier dysfunction independently from viral infection (33). Our work indicates that levels of S observed in clinical samples from COVID-19 patients are sufficient to mediate barrier dysfunction (250 ng/ml) (54, 55). Our findings suggest a contribution of integrins to COVID-19 pathology, in addition to functioning in S-mediated viral entry (18, 56). Further, our study offers a mechanistic explanation for the overproduction of TGF-β during COVID-19, which has been correlated with disease severity, and argues that this is a major trigger of vascular leak and barrier dysfunction associated with severe COVID-19 (57, 58). Thus, our work defines a new mechanism for S-triggered barrier dysfunction and vascular leak and uncovers potential new therapeutic avenues for COVID-19 treatment, targeting the role of S in pathogenesis in addition to its role in viral entry.

The source of S that interacts with endothelial and epithelial cells to mediate barrier dysfunction during SARS-CoV-2 infection is unclear, but our data suggest that virion-associated full-length S, soluble trimeric S, the recombinant RBD of S, and even cell-bound S (data not shown) are sufficient to mediate barrier dysfunction. Thus, we propose that SARS-CoV-2 can trigger barrier dysfunction through multiple avenues, including (1) during infection of virus-permissive cells, (2) through shedding of soluble S1 after enzymatic cleavage following ACE2 interactions on a cell, (3) through expression of S on the surface of infected cells that can interact with neighboring cells, and (4) through interactions with ACE2-negative non-permissive cells. Further investigation of clinical samples as well as *in vivo* experiments are required to explore these possibilities, which are essential to determine which species of S could be targeted for therapeutic intervention.

Based on our genetic data defining host factors required for S-mediated barrier dysfunction, we propose a model by which SARS-CoV-2 S first engages GAGs on the cell surface via positively charged surfaces in the RBD acquired specifically by SARS-CoV-2 (20). Once bound to the cell surface, S can engage integrins, such as α5β1 via a RGD integrin-binding motif within the RBD (18). Engagement of integrins can serve to displace LAP, which maintains TGF-β in an inactive state, thus resulting in the release of mature TGF-β that then engages the TGFBR to mediate signaling pathways regulating cell growth and transient barrier dysfunction **(Figure 7I)**. This compromise of barrier function is likely a result of activation of key enzymes such as HPSE, hyaluronidases, neuraminidases, MMP9, and ADAM17, which have distinct roles in disruption of the EGL and intercellular junctional complexes. Further, MMP9 and ADAM17 have separate reported roles in mediating maturation of TGF-β, and thus they may also contribute to S-mediated barrier dysfunction through this process (43, 44). While this investigation begins to shed light on the mechanisms by which SARS-CoV-2 S triggers barrier dysfunction, further studies are required to define additional host factors as well as to determine the relative contribution of each factor to this pathway.

Our study uncovers a new potential pathogenic role of S beyond ACE2 binding and viral entry, and many critical questions remain. First and foremost is how S-mediated barrier dysfunction influences outcome of SARS-CoV-2 infection. Previous data indicate that NS1-mediated vascular leak can exacerbate a sublethal DENV infection, providing a direct link to soluble NS1 promoting DENV pathogenesis (27, 59). In addition to inflammatory responses directly triggered by DENV NS1 (59), one hypothesis by which NS1 promotes pathogenesis is through facilitating dissemination of blood-borne flaviviruses from the blood and into distal tissues where the virus

9

can replicate to high titers (30, 33, 41, 60). Thus, we speculate that the contribution of S-mediated barrier dysfunction to COVID-19 pathogenesis is to promote dissemination of SARS-CoV-2 from the lung to the blood, and then into distal organs where virus-permissive cells reside. This is exemplified through the observation that administration of S into the lungs of mice results in systemic leak in the spleen and small intestine **(Figure 3)**. This could help explain the diverse clinical manifestations observed in COVID-19 patients. Further, the surface of the lungs is covered with a dense EGL comprising many glycans and proteoglycans, with a primary constituent being mucus composed of membrane-tethered and gel-forming mucins. It has been recently demonstrated that these mucins aid cells to be refractory to SARS-CoV-2 infection due to steric hindrance of virus-cell interactions; thus, S-mediated barrier dysfunction disrupting the EGL may make virus-permissive epithelial cells more accessible to invading virus (61, 62).

Our observation that S is sufficient to mediate endothelial dysfunction and vascular leak allows a direct comparison with the flavivirus NS1 protein. Such a comparison will contribute to our understanding of how viruses activate signaling pathways to mediate barrier dysfunction, and leads to the concept of development of pan-leak therapeutics that may be able to target pathology caused by multiple soluble viral proteins. Both similarities and distinctions are apparent in the mechanisms by which S and NS1 mediate endothelial barrier dysfunction (33). Our mechanistic investigation uncovered the contributions of GAGs (HS, CS, HA), MMP9, ADAM17, HPSE, integrins, and TGF-β signaling to S-mediated barrier dysfunction. GAG binding and activation of enzymes like MMP9, HPSE, hyaluronidase, and neuraminidases are common requirements for both NS1- and S-mediated endothelial dysfunction. In contrast, cathepsin L appears to be essential only for NS1 pathogenesis (28, 29), while S-mediated dysfunction requires engagement of integrins and TGF-β signaling. These differences may explain the distinct kinetics of our *in vitro* hyperpermeability assays, with NS1 causing a peak of leak ~6 hours post-NS1 treatment while the S-mediated peak of leak occurs ~24 hpt with no perturbation of barrier function observed at 6 hpt. One potential reason for this may be due to the requirement for TGF-β production and signaling as a second messenger for S-mediated endothelial dysfunction, which is not required for flavivirus NS1-induced leak. Further comparative investigations between the mechanisms of S- and NS1-mediated barrier dysfunction are needed to fully understand what makes these pathways activated by SARS-CoV-2 S and flavivirus NS1 similar yet distinct which will be critical for development of pan-viral anti-barrier permeability therapeutics.

It is important to note that our working hypothesis is not that S mediates disease pathogenesis alone, but rather that the reversible vascular leak triggered by S serves to promote viral dissemination of SARS-CoV-2 into distal tissues of infected patients, which can lead to severe disease manifestations. Indeed, although we observe significant vascular leak in mice administered S, they do not overtly display signs of morbidity. Importantly, our findings suggest that the amounts of S circulating in patients following COVID vaccination (pg/mL levels) are too low to trigger vascular leak given that our phenotype requires ng-µg/mL levels that mimic the levels observed during severe COVID-19 cases (54, 55). Taken together, our study and available literature (63) indicate that S-mediated vascular leak would not result from COVID-19 vaccination and therefore it is not correlated with vaccine adverse events.

In sum, our study reveals the role of S in COVID-19-associated pathologies such as vascular leak and provides mechanistic insight into how S mediates pathology independently from viral infection and the ACE2 receptor, suggesting that therapeutics that blockade interactions between S and GAGs, integrins, or the TGF-β-signaling axis may serve to decrease COVID-19 disease severity

through inhibition of a SARS-CoV-2 virulence factor, or viral toxin, as has been demonstrated for flavivirus NS1 (35, 64). Although much work remains to be done to fully understand the structural basis of this mechanism as well as the evolutionary implications for this pathway in pathogenesis in humans during SARS-CoV-2 infection and even infection of future emerging viruses, this work provides a foundation for future investigations by beginning to define the contribution of S to COVID-19-associated vascular leak.

Acknowledgements

Author Contributions

Conceptualization: S.B.B., F.T.G.S., P.R.B., E.H.; Funding acquisition: J.E.P., E.H.; Investigation: S.B.B., F.T.G.S., L.V.T., F.P., R.R., S.F.B., T.S.P., D.R.G., B.C.R., V.S., Ca.M.W., N.T.N.L., M.P.W., Co.M.W., D.R.S., T.M.C., Y.A.S., V.O.; Methodology: S.B.B., F.T.G.S., L.T., F.P., R.R., S.F.B., T.P., D.R.G., D.R.S., T.M.C., V.O., P.R.B., E.H.; Project administration: E.H.; Supervision: S.B.B., H.C.A., J.D.E., C.Y.C., J.E.P., E.H.; Visualization: S.B.B., F.T.G.S., L.T., F.P., D.R.G., V.S., E.H.; Writing – original draft: S.B.B., F.T.G.S., E.H.; Writing – review & editing: S.B.B., F.T.G.S., F.P., P.R.B., E.H.

Declarations of Interest

The authors declare no competing interests.

Figures
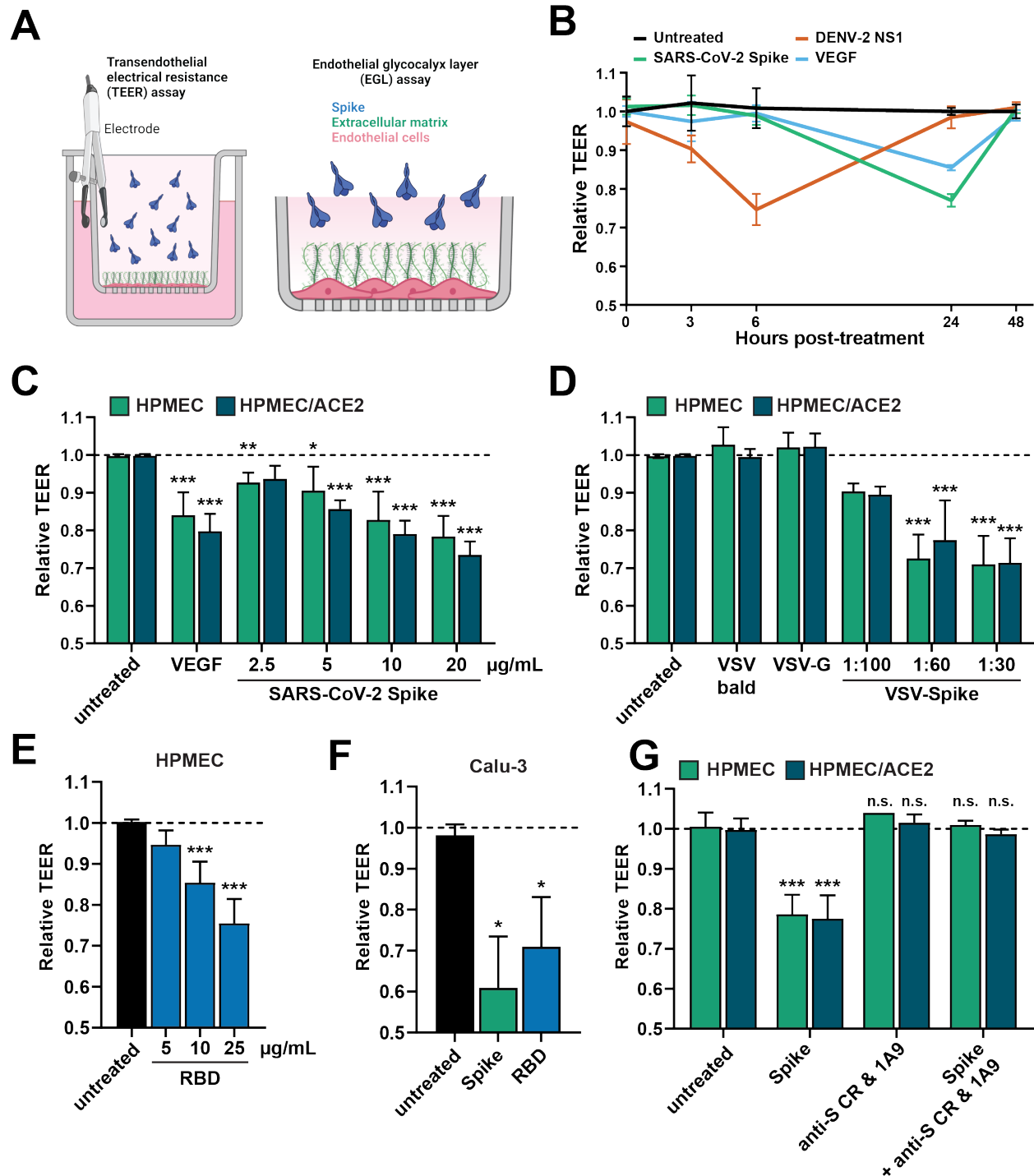
Figure 1. SARS-CoV-2 S triggers endothelial and epithelial barrier hyperpermeability. (A) Schematic depicting S-triggered barrier dysfunction measured by a trans-endothelial/epithelial electrical resistance assay (TEER; left) and an endo/epithelial glycocalyx layer (EGL) assay (right). **(B)** Time course TEER assay measuring the barrier function of HPMEC monolayers over time with the indicated treatments, including DENV2 NS1 (5 µg/mL), VEGF (50 ng/mL), and

SARS-CoV-2 S (10 μg/mL). Data are from n=2 biological replicates. **(C)** A TEER assay measuring the barrier of monolayers of HPMEC and HPMEC/ACE2 at 24 hours after the indicated treatments. VEGF positive control (50 ng/mL). Data are from n=3 biological replicates. **(D)** Same as C but treated with the indicated VSV pseudotyped particles at the indicated dilutions. VSV-bald and VSV-G are diluted 1:30. Data are from n=3 biological replicates. **(E)** Same as C but treated with the indicated concentrations of SARS-CoV-2 RBD. Data are from n=3 biological replicates. **(F)** Same as C but measuring the barrier of Calu-3 cell monolayers. Data are from n=2 biological replicates. **(G)** A TEER inhibition assay measuring the capacity of a cocktail of anti-S antibodies to inhibit S-mediated endothelial hyperpermeability. S (10 μg/mL) and the antibody cocktail (15 μg/mL for each antibody; 1A9 [Genetex] and CR3022 [Absolute Antibody]) were added simultaneously to the upper chamber of transwell inserts to a monolayer of HPMEC or HPMEC/ACE2 and TEER was measured 24 hours post-treatment (hpt). Data are from n=2 biological replicates. In all panels, the dotted line is the normalized TEER value of the untreated control condition. All data are plotted as mean +/- SD. For all panels, values are compared to untreated controls by ANOVA with multiple comparisons with *p<0.05, **p<0.01, ***p<0.001, and n.s. p>0.05.
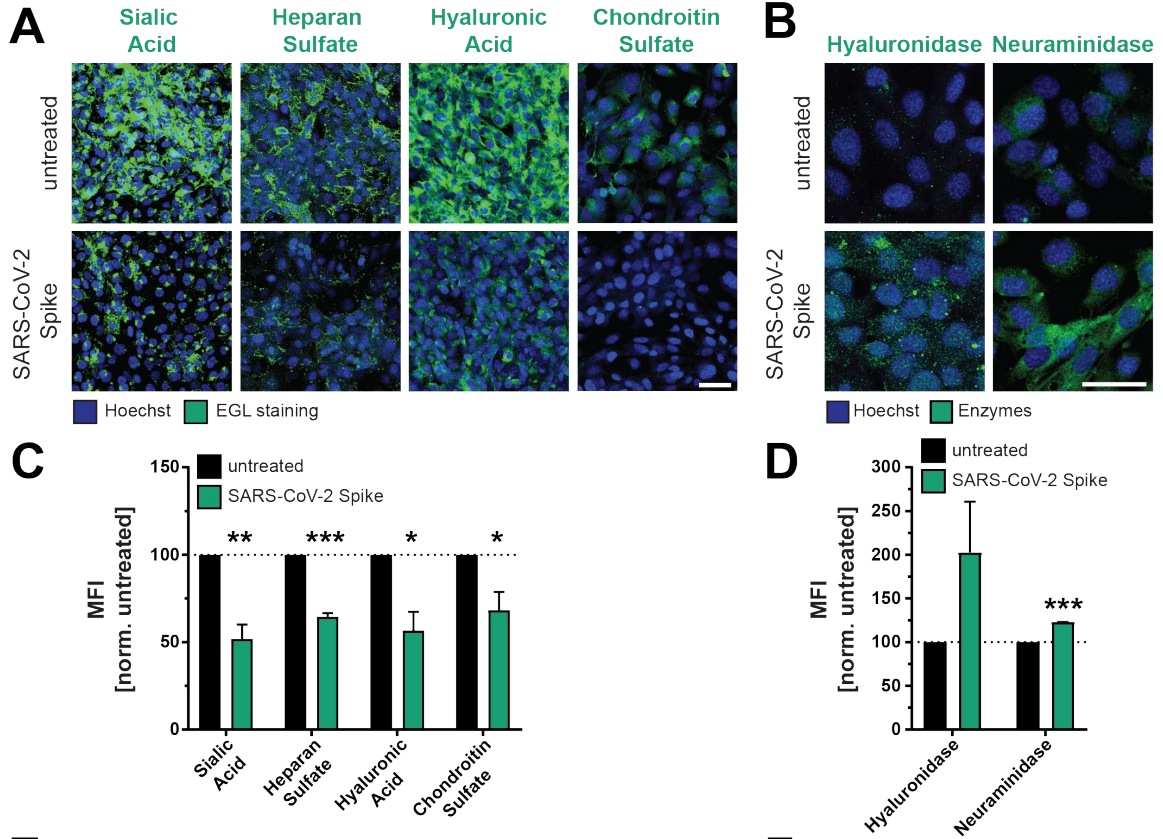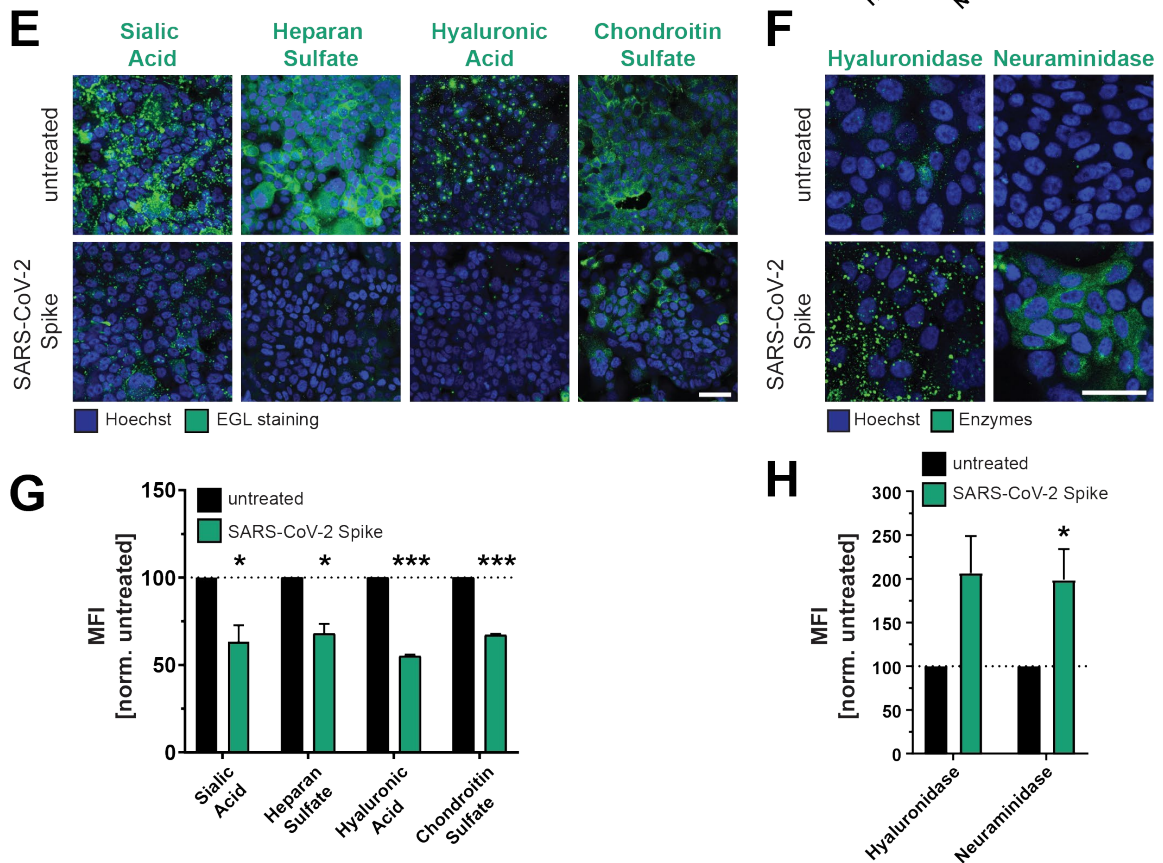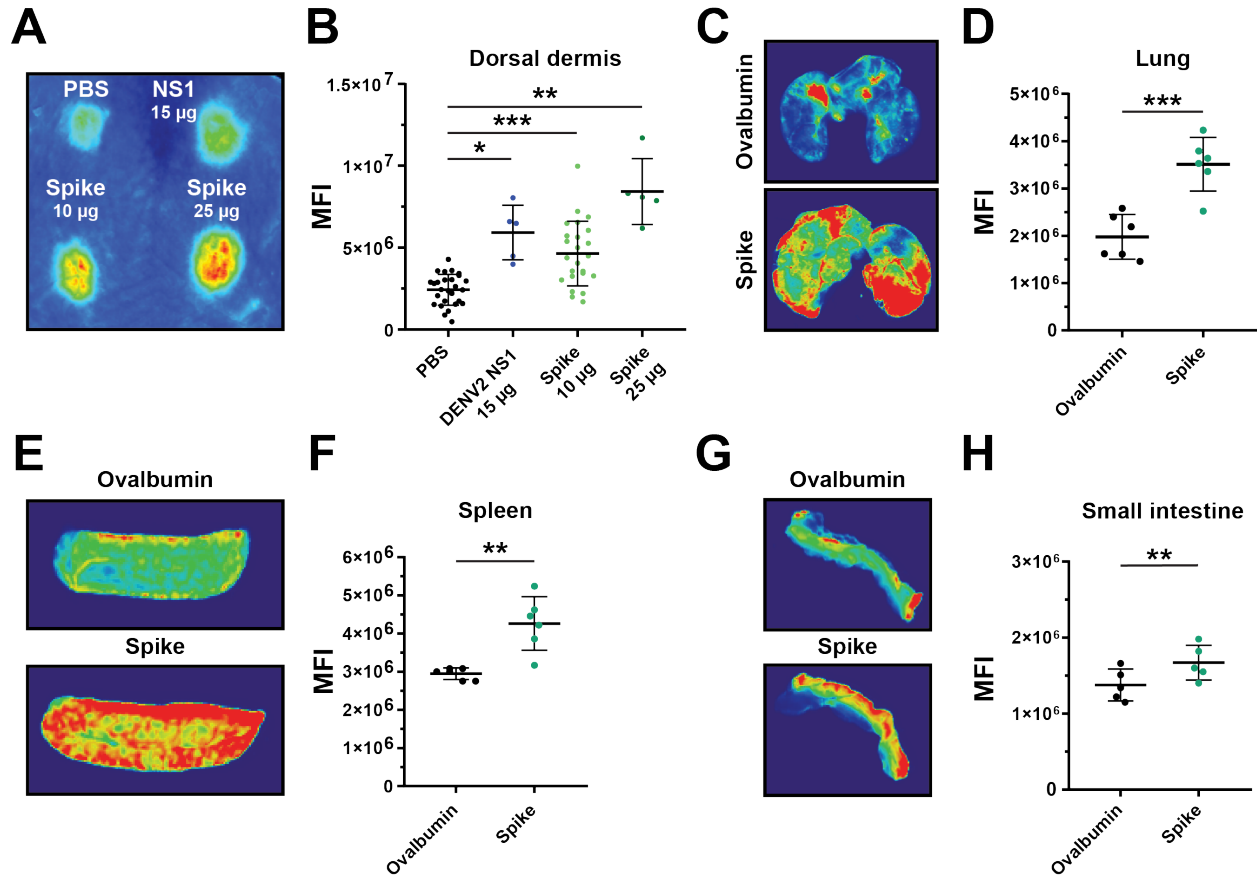
Figure 2. SARS-CoV-2 S facilitates disruption of the endothelial and epithelial glycocalyx layer. (A) An immunofluorescence microscopy-based EGL disruption assay measuring levels of the indicated glycans on the surface of HPMEC. After 24 h of SARS-CoV-2 S (10 µg/mL) treatment, cells were fixed then stained without permeabilization. Displayed are representative images from n=3 biological replicates. **(B)** Same as A, but cells were permeabilized before staining for the indicated EGL disrupting enzymes. Displayed are representative images from n=3 biological replicates. **(C)** Quantification of A. **(D)** Quantification of B. **(E)** Same as A but measuring EGL disruption of Calu-3 cell monolayers. Displayed are representative images from n=3 biological replicates. **(F)** Same as B but measuring expression of EGL-disrupting enzymes in Calu-3 cells. Displayed are representative images from n=3 biological replicates. **(G)** Quantification of E. **(H)** Quantification of F. For all images, nuclei were probed with Hoechst in blue and the indicated glycans in green with scale bars at 100 µm. Dotted lines are the normalized untreated control conditions. MFI is mean fluorescence intensity. All data are plotted as mean +/- SEM with * $p<0.05$, ** $p<0.01$, *** $p<0.001$, and n.s. $p>0.05$ by unpaired t-test.

Figure 3. SARS-CoV-2 S triggers vascular leak *in vivo*. (A) A representative mouse back from a dermal leak experiment. The dorsal dermises of mice were injected intradermally with the treatments and doses indicated. Mice then received a dextran-680 tracer molecule intravenously. Mouse dermises were collected 2 h post-treatment and quantification of local dermal leak was assessed by a fluorescent scanner. **(B)** Quantification of A from mice treated with PBS (n=27), DENV2 NS1 (15 µg; n=5), S (10 µg; n=25), and S (25 µg; n=5). **(C)** Representative lung images from a SARS-CoV-2 S systemic vascular leak assay. Mice were administered 50 µg of SARS-CoV-2 S or ovalbumin intranasally as indicated, and 22 hpt were administered a dextran-680 tracer intravenously as in A. Organs of mice were collected 2 hours post dextran-680 administration (24 hours post-S treatment), and accumulation of dextran-680 was measured with a fluorescent scanner. **(D)** Quantification of C from n=6 mice. **(E)** Same as C except representative images of spleens. **(F)** Quantification of E from n=6 mice. **(G)** Same as C except representative images of small intestine. **(H)** Quantification of G from n=5 mice. MFI is mean fluorescence intensity. All data are plotted as mean +/- SEM with *p<0.05, **p<0.01, and ***p<0.001 by unpaired t-test.
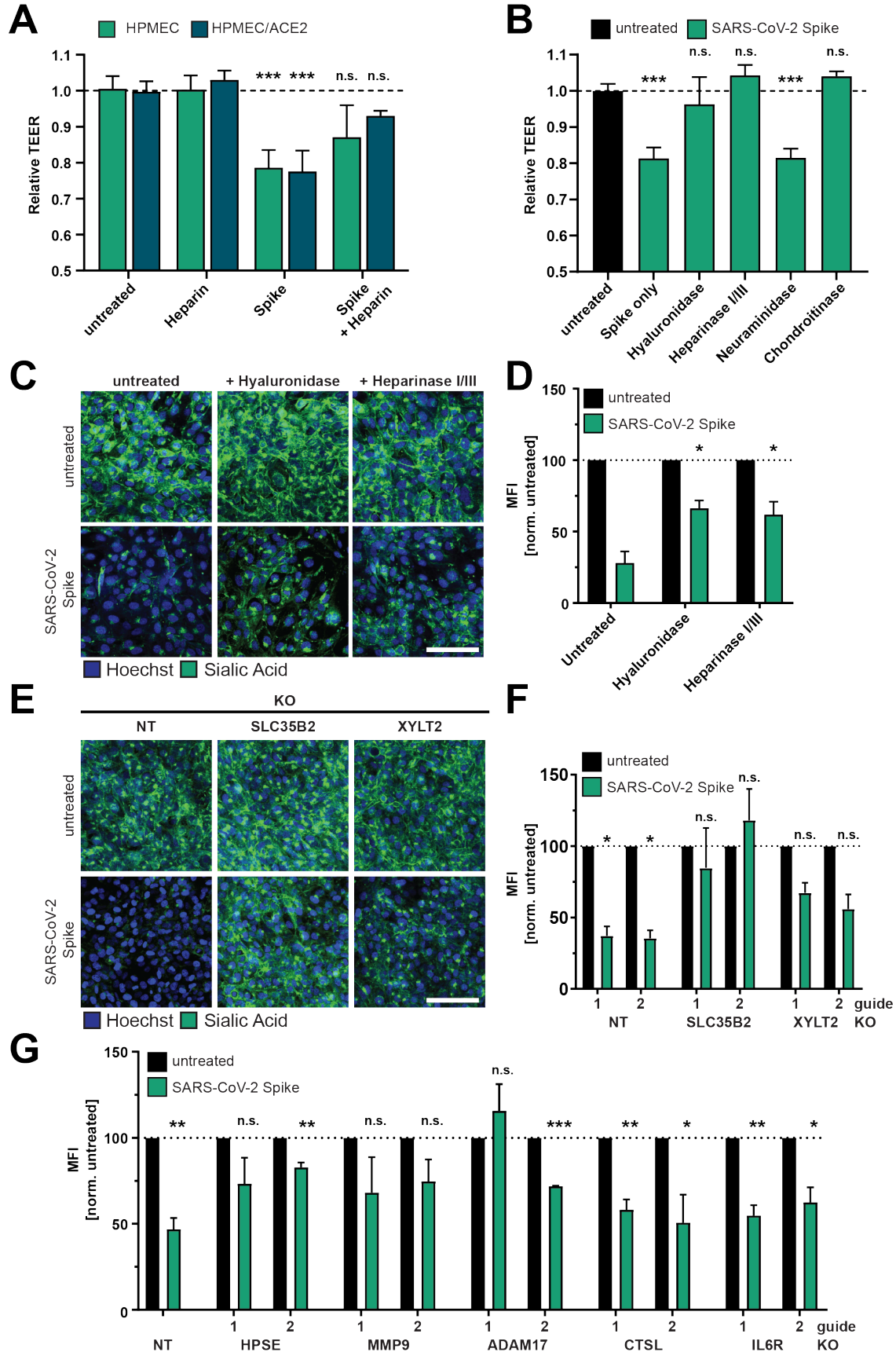
16

Figure 4. Glycosaminoglycans and EGL modulating enzymes are required for SARS-CoV-2 S-mediated barrier dysfunction. (A) TEER inhibition assay on monolayers of HPMEC or HPMEC/ACE2 treated with heparin (10 µg/mL), S (10 µg/mL), or both simultaneously. TEER readings were taken 24 hpt. Data are from n=2 biological replicates. **(B)** A TEER inhibition assay where monolayers of HPMEC were treated with recombinant hyaluronidase (10 µg/mL), heparin lyases I and III (5 mU/mL each), neuraminidase (1 U/mL), or chondroitinase (25 mU/mL) simultaneously with S (10 µg/mL) treatment. TEER readings were taken 24 hpt. Data are from n=2 biological replicates. **(C)** EGL inhibition assay on HPMEC treated with hyaluronidase (10 µg/mL) or heparin lyases I and III (5 mU/mL each) and simultaneously treated with S (10 µg/mL) and fixed 24 hpt. **(D)** Quantification of C from n=2 biological replicates. Statistics are comparisons of indicated conditions to the S-only control condition. **(E)** Representative images from an EGL disruption assay of HPMEC transduced with lentiviruses encoding the indicated gene-targeting guide RNA. Cells were treated with 10 µg/mL S, and sialic acid was visualized by IFA 24 hpt. **(F)** Quantification of E from n=3 biological replicates. Control guide data from this panel are from the same experiment as Figure S1G. **(G)** Same as E and F but using the indicated guide RNAs. Non-target (NT) data are pooled from two cell line replicates. Control guide data from this panel are from the same experiments as Figure 7G. For all panels, sialic acid is stained with Wheat Germ Agglutinin in green and nuclei are stained with Hoechst in blue with scale bars at 100 µm. MFI is mean fluorescence intensity. Dotted lines are the normalized untreated control conditions. All data are plotted as mean +/- SD (TEER) or SEM (EGL) with *p<0.05, **p<0.01, ***p<0.001, and n.s. p>0.05 by ANOVA with multiple comparisons.
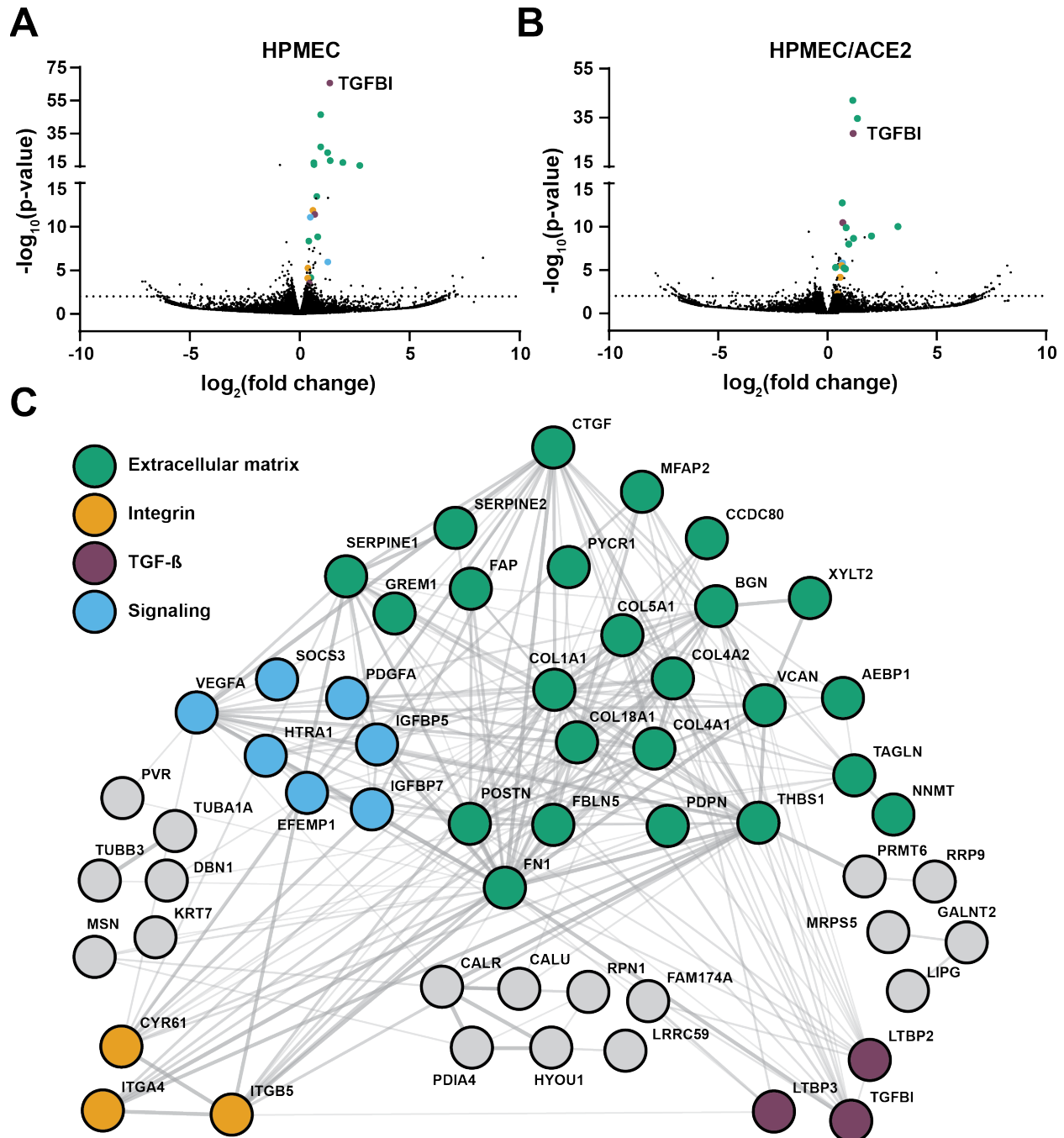
18

Figure 5. RNA-Sequencing analysis of SARS-CoV-2 S-treated HPMEC and HPMEC/ACE2. **(A)** A volcano plot of differentially expressed genes (DEGs) detected in HPMEC treated with 10 µg/mL of SARS-CoV-2 S at 24 hpt. **(B)** Same as A but displaying DEGs from HPMEC/ACE2 treated with 10 µg/mL SARS-CoV-2 S. Dotted lines indicate the threshold for significance. **(C)** A STRING protein-protein interaction network of DEGs identified between S-treated and untreated conditions for HPMEC.
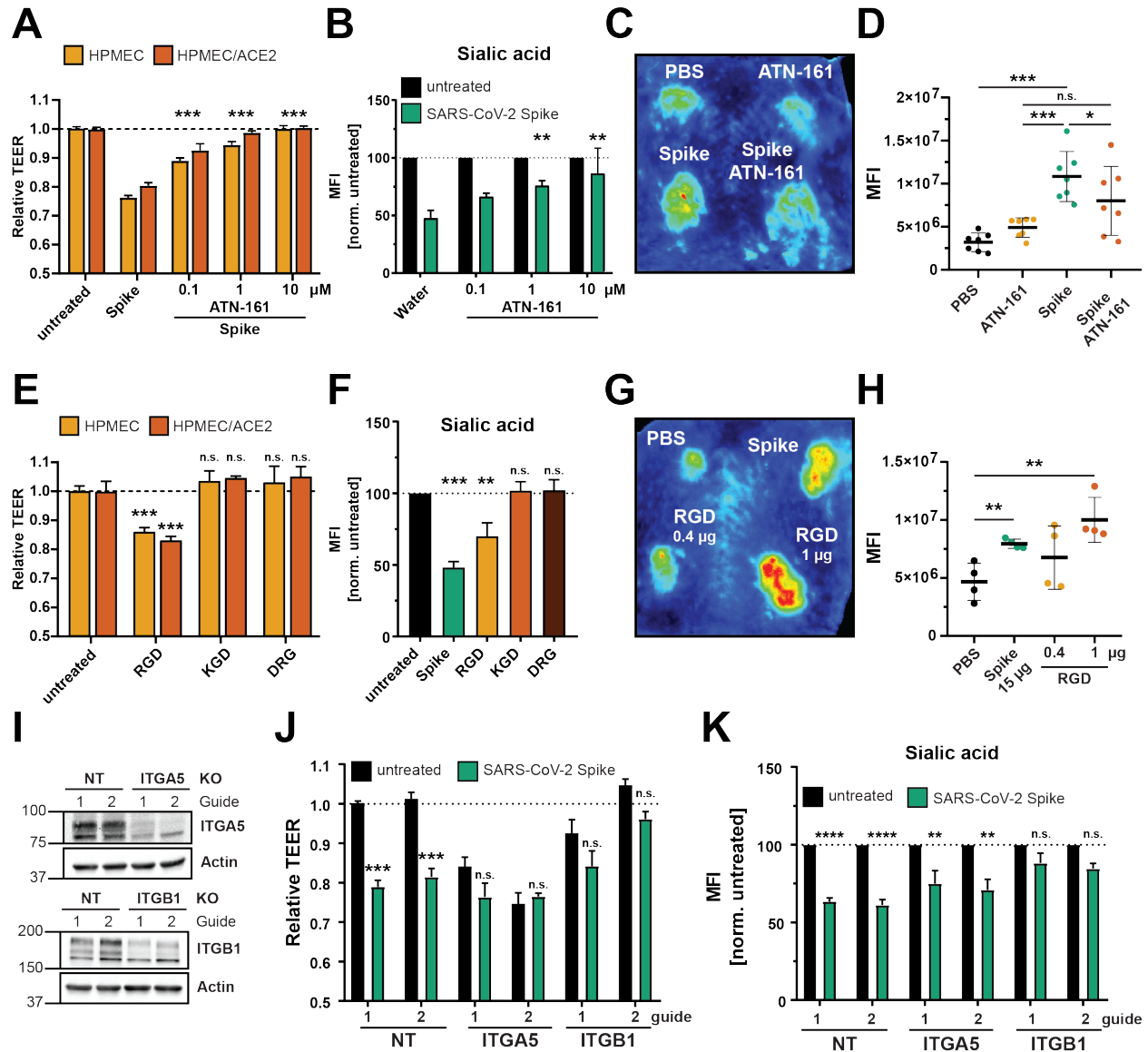
Figure 6. Integrins are required for SARS-CoV-2 S-mediated endothelial barrier dysfunction. (A) TEER inhibition assay of HPMEC and HPMEC/ACE2 monolayers treated with S (10 µg/mL) and the indicated concentrations of the integrin inhibitor ATN-161. TEER readings were taken 24 hpt with ATN-161 and S added simultaneously to cells. Data are from n=2 biological replicates. **(B)** EGL inhibition assay detecting sialic acid on the surface of HPMEC monolayers treated with S and ATN-161 as in A. Data are from at least n=2 biological replicates. **(C)** Representative back from an intradermal leak assay of mice with the indicated treatments; S (10 µg/mL) and ATN-161 (1 µM) injected simultaneously. **(D)** Quantification of C from n=7 mice. **(E)** TEER assay of HPMEC and HPMEC/ACE2 monolayers treated with the indicated peptides at 0.4 µM. TEER readings were taken 24 hpt. Data are from n=2 biological replicates. **(F)** Same as E, but an EGL assay detecting sialic acid on the surface of HPMEC monolayers. Data are from n=3 biological replicates. **(G)** Representative back from an intradermal leak assay of mice with the indicated treatments with S (10 µg/mL) and the indicated doses of RGD peptide. **(H)** Quantification of G from n=4 mice**. (I)** Western blot analysis of HPMEC transduced with the indicated lentivirus-

encoding guide RNA. Actin was used as a loading control. **(J)** TEER assay of HPMEC transduced with lentivirus-encoding guide RNAs targeting the indicated genes as in I. Cell were treated with 10 µg/mL of S and TEER was read 24 hpt. Data are from n=2 biological replicates. **(K)** EGL assay detecting sialic acid on the cell surface of transduced HPMECs as in J. Data are from n=3 biological replicates. MFI is mean fluorescence intensity. Dotted lines are the normalized untreated control conditions. All data are as plotted as mean +/- SD (TEER) or SEM (EGL) with *p<0.05, **p<0.01, ***p<0.001, and n.s. p>0.05 by ANOVA with multiple comparisons.
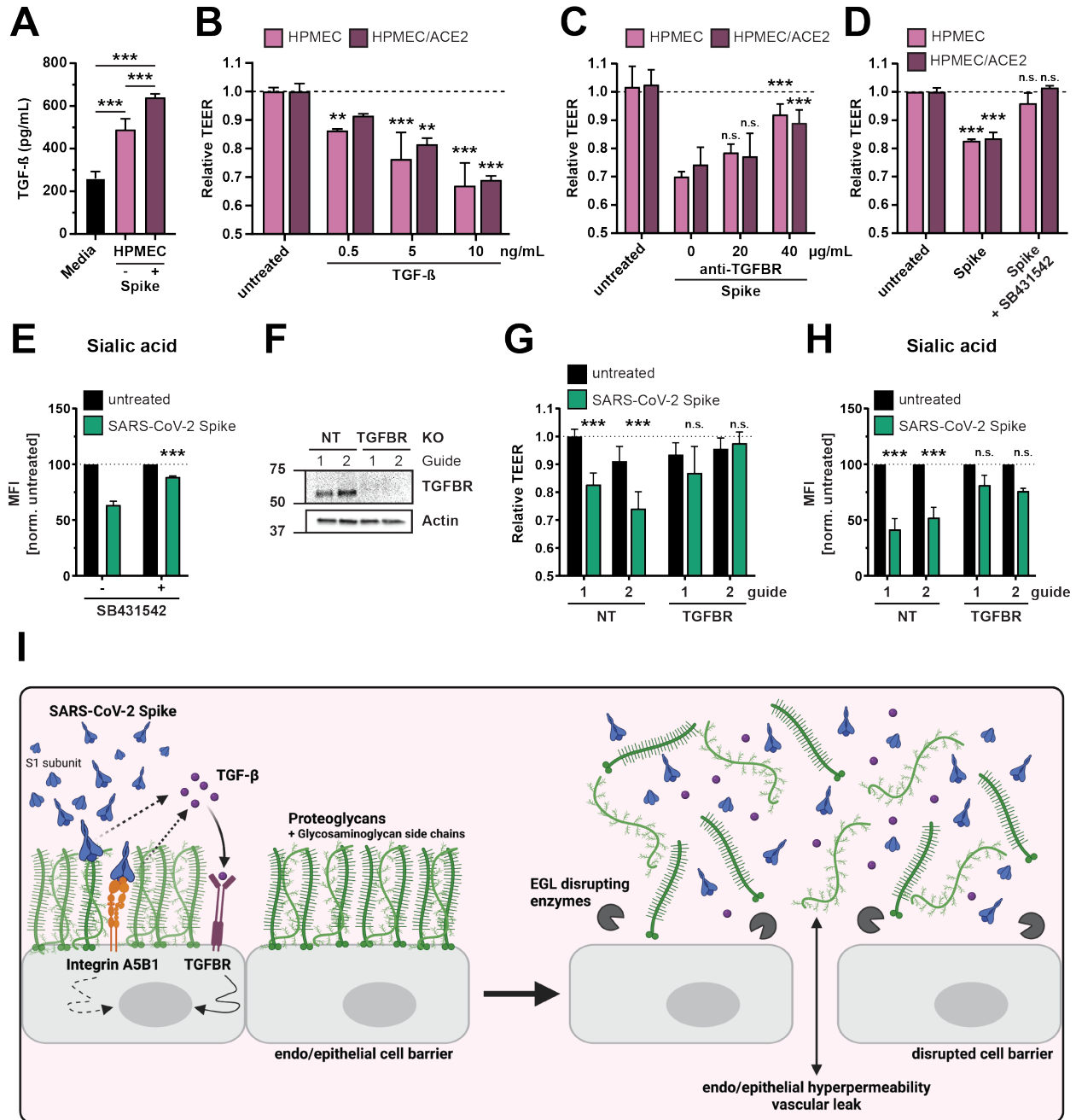
Figure 7. SARS-CoV-2 S triggers production of TGF-β, and TGF-β signaling is required for S-mediated barrier dysfunction (A) Commercial ELISA detecting TGF-β in medium without cell conditioning (Media), medium from untreated HPMEC, and medium from HPMEC treated with 10 µg/mL SARS-CoV-2 S. Data are from n=3 biological replicates. **(B)** TEER assay measuring the effect of recombinant TGF-β on barrier function of HPMEC at the indicated concentrations. TEER readings were taken 24 hpt. Data are from n=2 biological replicates. **(C)** TEER assay measuring the capacity of an anti-TGFBR antibody, at the indicated concentrations, to abrogate S-mediated (10 µg/mL) endothelial hyperpermeability of HPMEC and HPMEC/ACE2. TEER readings were taken 24 hpt. Data are from n=2 biological replicates. **(D)** TEER assay measuring the capacity of TGFBR inhibitor SB431542 (1 µM) to inhibit S (10 µg/mL) function. Data are from n=2 biological

22

replicates. **(E)** Same as D, except an EGL assay measuring sialic acid. Data are from n=3 biological replicates. **(F)** Western blot analysis of HPMEC transduced with lentivirus-encoding guide RNAs targeting the indicated genes. Actin was used as a loading control. Data are one representative experiment from n=3 biological replicates. **(G)** TEER assay on the same HPMEC as in F treated with 10 μg/mL of S and measured 24 hpt. Data are from n=3 biological replicates. **(H)** EGL disruption assay on HPMECs from F, treated with 10 μg/mL S and imaged 24 hpt. Control guide data from this panel are from the same experiment as Figure 4G. Data are from n=3 biological replicates. **(I)** Graphical abstract summarizing the ACE2-independent pathway by which SARS-CoV-2 S triggers barrier dysfunction. Interactions with proteoglycans, glycosaminoglycans, and integrins are required for S-mediated release of TGF-β, which is required for S-mediated barrier dysfunction via TGFBR signaling. Solid lines represent steps with direct experimental evidence while dotted lines represent hypothesized steps. For all figures, dotted lines in graphs are the normalized untreated control conditions. MFI is mean fluorescence intensity. All data are plotted as mean +/- SD (TEER) and SEM (EGL) with *p<0.05, **p<0.01, ***p<0.001, and n.s. p>0.05 by ANOVA with multiple comparisons.
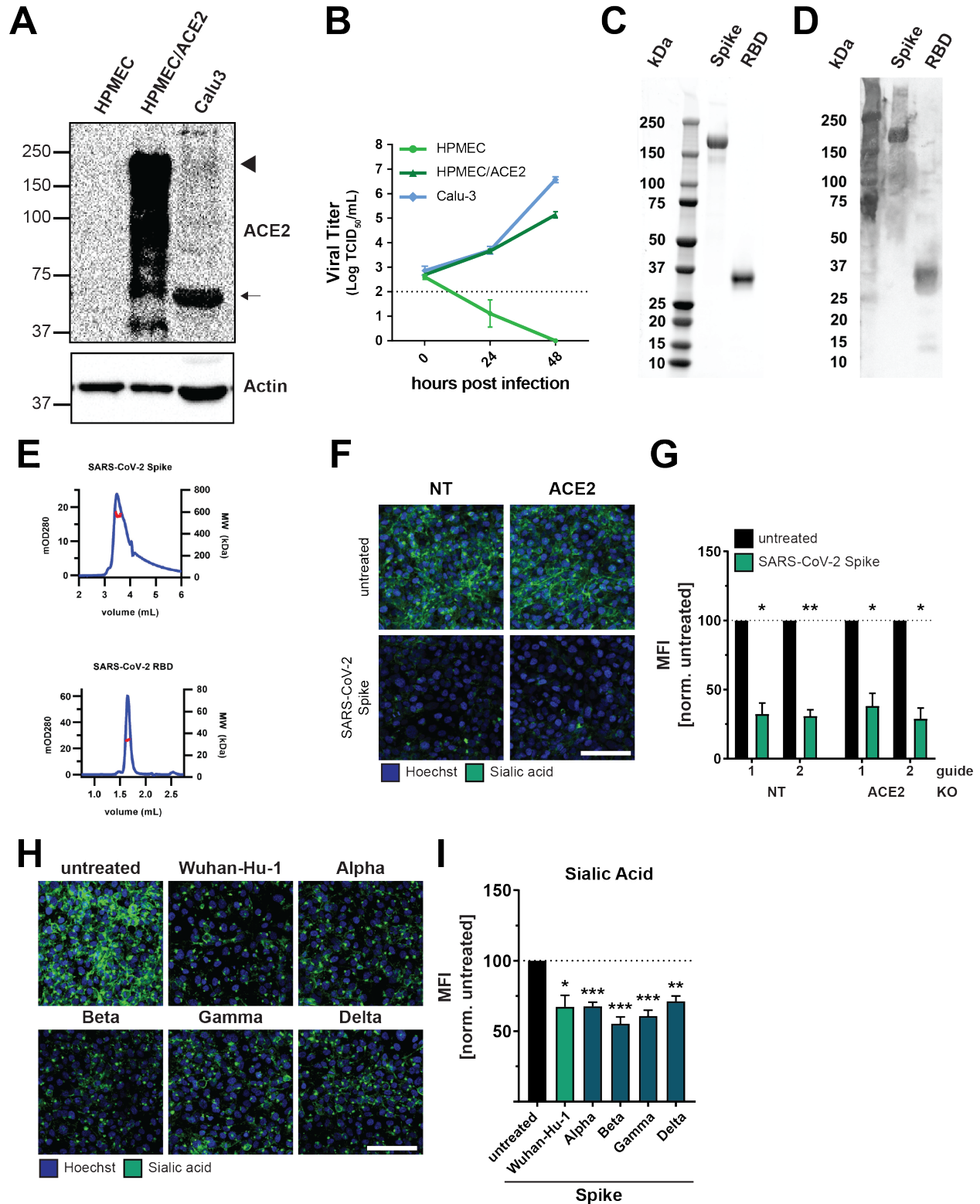
Supplemental Figures

Figure S1. In-house produced S is pure and mediates barrier dysfunction in an ACE2-independent manner (Related to Figure 1 and Figure 2). (A) Western blot analysis of ACE2

expression in HPMEC, HPMEC/ACE2, and Calu-3 cells. The arrowhead points to the predicted size of ACE2, while the arrow points to a smaller truncated band. Actin was used as a loading control. Shown is one representative experiment from n=3 biological replicates. **(B)** Growth curve of HPMEC, HPMEC/ACE2, and Calu-3 cells infected with SARS-CoV-2 at an MOI of 0.005, titered by $TCID_{50}$ at the indicated time-points. Data displayed are from n=3 biological replicates. The dotted line is the limit of detection (LOD) of the assay. **(C)** Western blot analysis of home-made full-length trimeric spike and RBD detected by an anti-6xHIS antibody. **(D)** SDS-PAGE visualized by silver stain of home-made full-length trimeric spike and RBD. **(E)** Size-exclusion chromatography of in-house-produced full-length trimeric spike (top) and RBD (bottom). **(F)** Sialic acid EGL assay on HPMEC transduced with lentivirus-encoding guide RNAs targeting the indicated genes, treated with 10 µg/mL of S and imaged at 24 hpt. Shown are representative images from n=3 biological replicates. **(G)** Quantification of F; Control guide data from this panel are from the same experiment as Figure 4F. **(H)** Sialic acid EGL disruption assay of HPMEC treated with SARS-CoV-2 S (10 µg/ml) from the indicated variants. Data are from n=3 biological replicates. **(I)** Quantification of H. For all panels, sialic acid is stained in green and nuclei are stained with Hoechst in blue with scale bars at 100 µm. MFI is mean fluorescence intensity. Dotted lines are the normalized untreated control conditions. All data are plotted as mean +/- SEM with *$p<0.05$, **$p<0.01$, ***$p<0.001$, and n.s. $p>0.05$ by ANOVA with multiple comparisons.
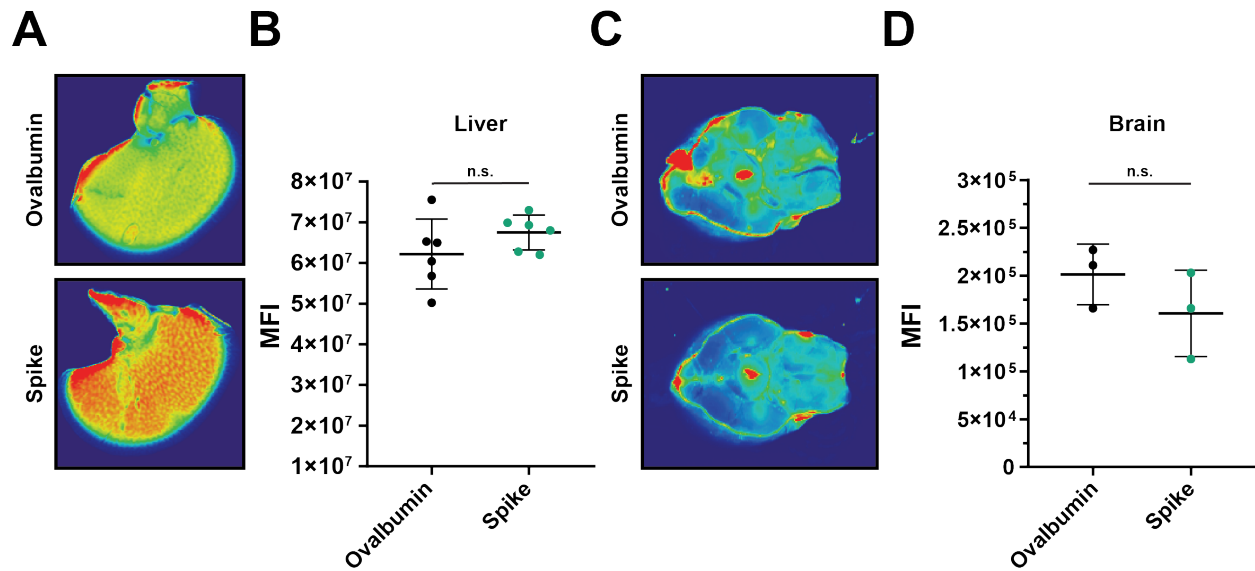
Figure S2. SARS-CoV-2 S triggers vascular leak *in vivo* (Related to Figure 3). (A) Representative liver images from a SARS-CoV-2 S systemic vascular leak assay. Mice were administered 50 µg of SARS-CoV-2 S or ovalbumin as indicated, and 24 hpt were administered dextran-680 intravenously as in Figure 3. Organs from mice were collected, and accumulation of dextran-680 was measured with a fluorescent scanner. **(B)** Quantification of A from n=6 mice. **(C)** Same as A except representative images of brains. **(D)** Quantification of C from n=3 mice.
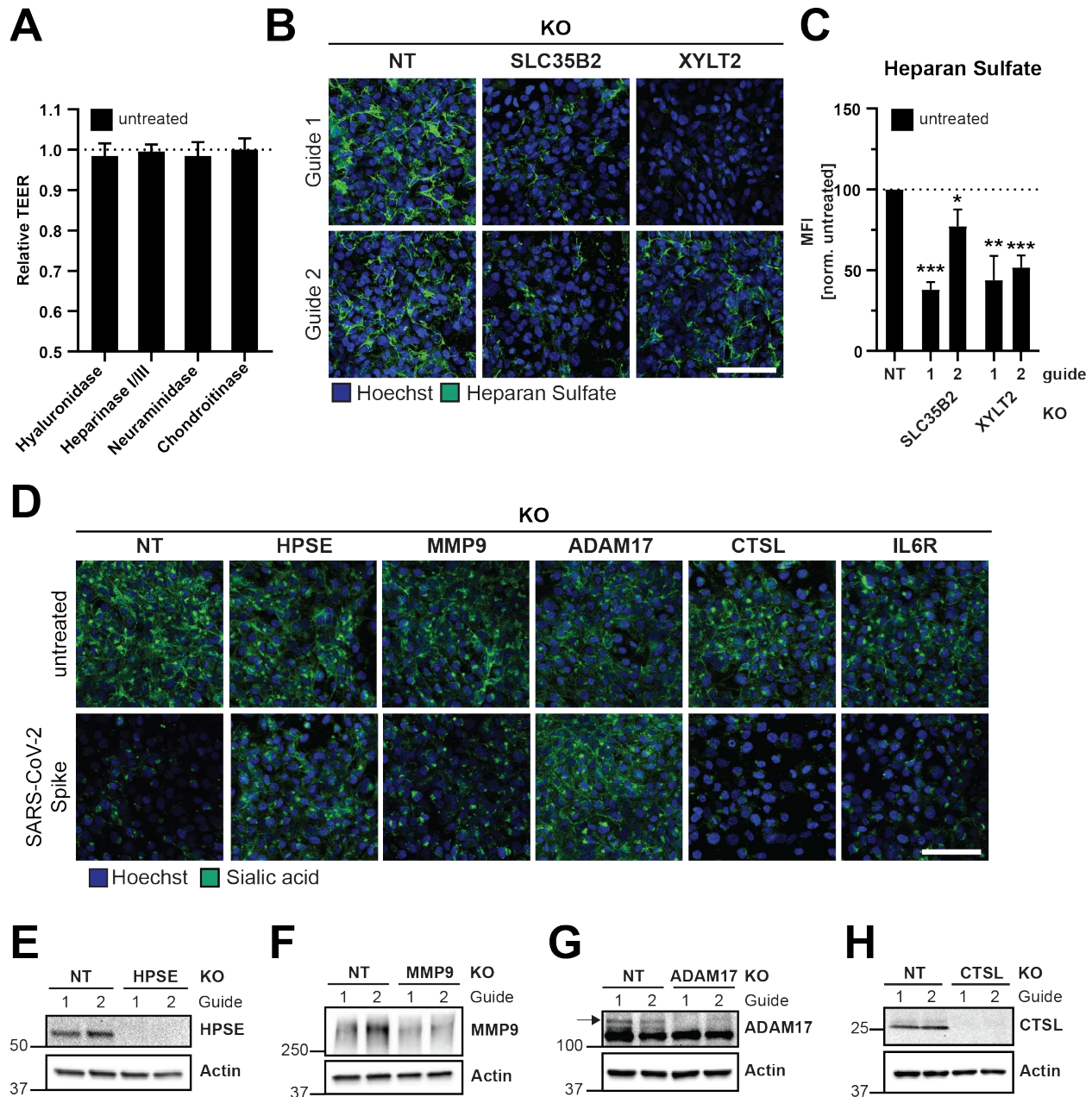
Figure S3. Glycans and EGL-modifying enzymes are required for S-mediated barrier dysfunction (Related to Figure 4). (A) TEER assay of HPMEC treated with recombinant hyaluronidase (10 μg/mL), heparin lyases I and III (5 mU/mL each), neuraminidase (1 U/mL), or chondroitinase (25 mU/mL). Data presented are control conditions from Figure 4B. Data are from n=2 biological replicates. **(B)** Representative IFA images of HPMEC transduced with lentivirus encoding the indicated guide RNAs and stained for heparan sulfate. Data presented are controls for Figure 4E. Displayed is one representative image from n=3 biological replicates. **(C)** Quantification of C. **(D)** A sialic acid EGL assay of HPMEC transduced with lentivirus encoding the indicated guide RNAs. HPMECs were treated with S (10 μg/mL) and stained 24 hours post-treatment. Data are representative IFA images from Figure 4G with n=3 biological replicates. **(E-H)** Western blot analyses for HPMECs from Figure 4G and Figure S3D probed for **(E)** heparanase

27

(HPSE), **(F)** matrix metalloproteinase 9 (MMP9), **(G)** a disintegrin and metalloprotease 17 (ADAM17), and **(H)** Cathepsin L (CTSL). Actin was used as a loading control for all. All blots are from at least n=2 biological replicates. For all panels, heparan sulfate or sialic acid are stained in green and nuclei are stained with Hoechst in blue with scale bars at 100 μm. MFI is mean fluorescence intensity. All data are plotted as mean +/- SD (TEER) or SEM (EGL) with *$p<0.05$, **$p<0.01$, ***$p<0.001$, and n.s. $p>0.05$ by ANOVA with multiple comparisons.
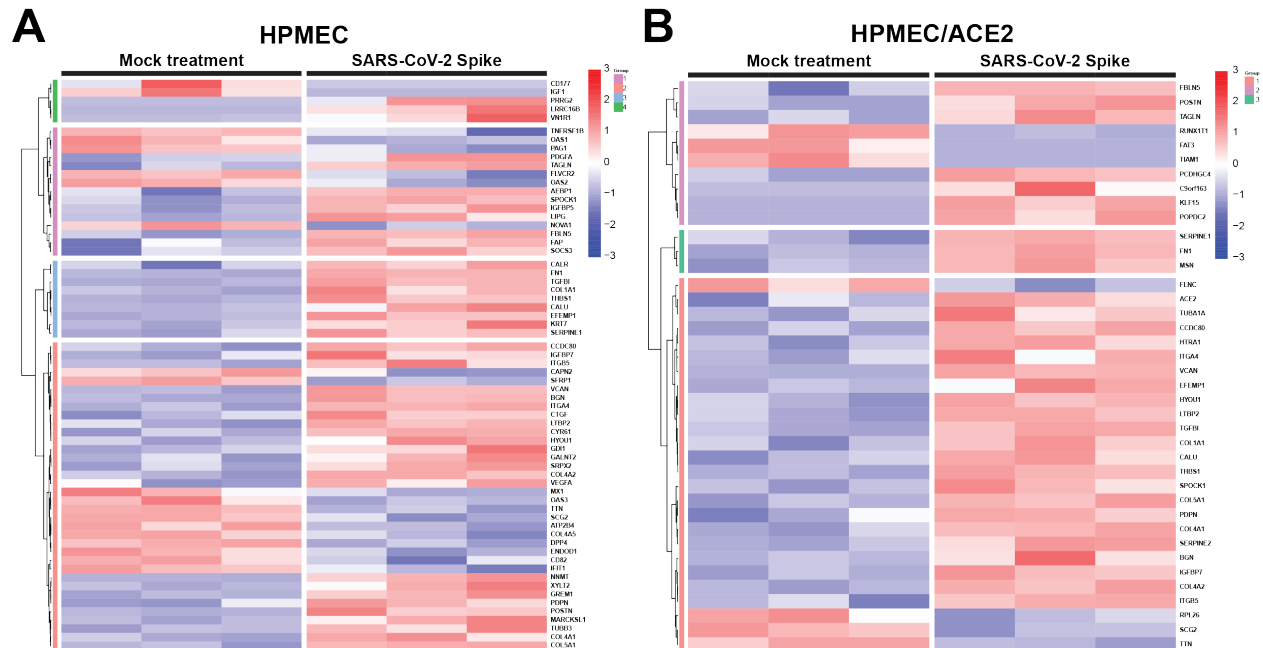
Figure S4. RNA-Seq of HPMEC and HPMEC/ACE2 treated with SARS-CoV-2 S (Related to Figure 5). (A) Heat map of DEGs identified in HPMEC treated with 10 µg/mL S for 24 hours. **(B)** Same as A except HPMEC/ACE2. The group designation refers to the cluster where the gene belongs after performing unsupervised hierarchical clustering. The color scale represents the z-score of normalized gene expression values. DEGs with BH-corrected p value <0.05 were included.

Figure S5. Integrins are required for SARS-CoV-2 S-mediated barrier dysfunction. (Related to Figure 6). (A) TEER assay of HPMEC treated with the indicated concentration of the integrin inhibitor ATN-161 for 24 hours. Dotted line is the normalized untreated control condition. These data are controls from Figure 6A and are from n=2 biological replicates. **(B)** Sialic acid EGL assay of HPMEC treated with 10 µg/mL of S and the indicated concentration of ATN-161. EGL was visualized 24 hpt. Data are representative images from Figure 6B and from at least n=2 biological replicates. **(C)** Sialic acid EGL assay as in B but treated with the indicated small peptides at 0.4 µM or S at 10 µg/mL. Data are representative images from Figure 6F from n=3 biological replicates. **(D)** Sialic acid EGL assay as in B but with the indicated CRISPR KO HPMECs. Data are representative images from Figure 6K with n=3 biological replicates. For all panels, sialic acid is stained in green and nuclei are stained with Hoechst in blue with scale bars at 100 µm. All data are plotted as mean +/- SD.
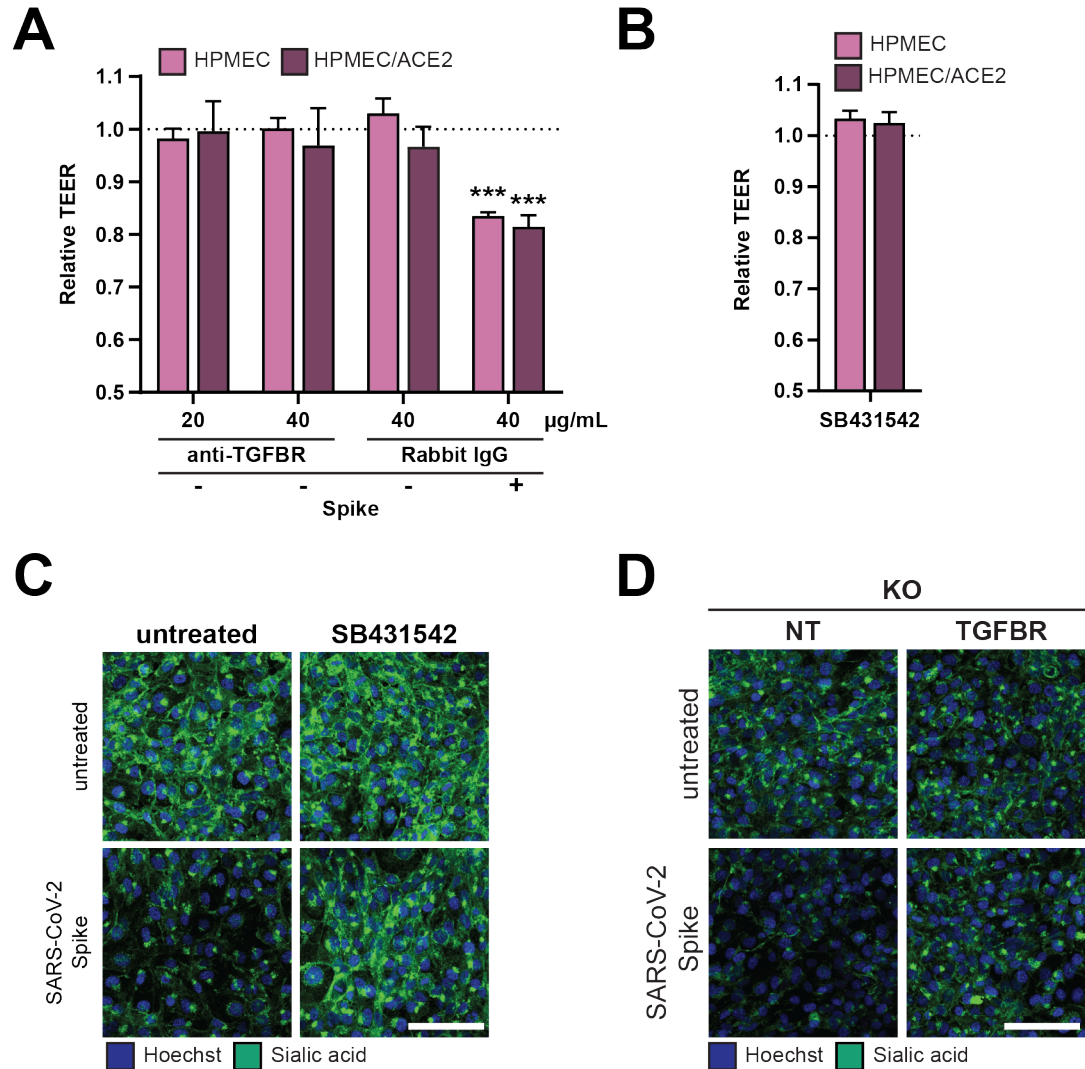
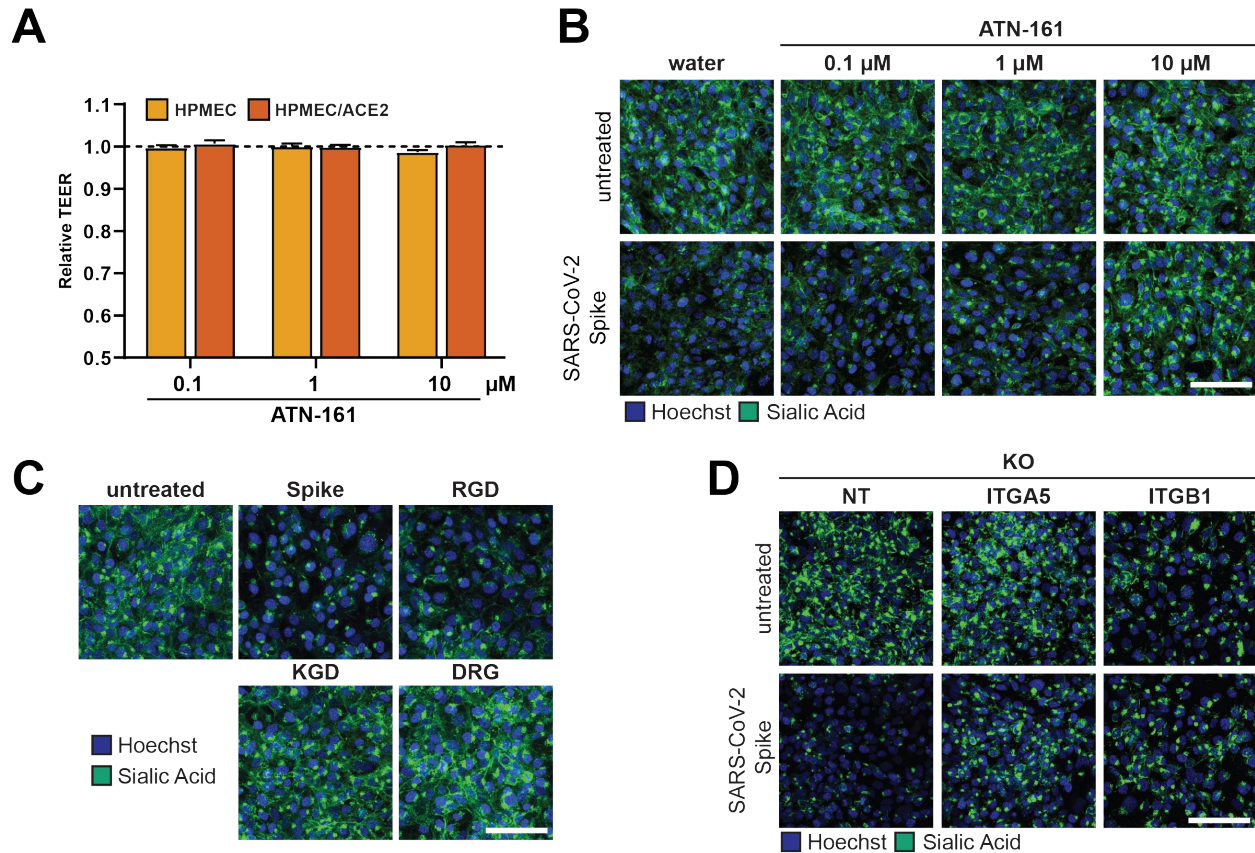**Figure S6. TGF-β signaling is required for SARS-CoV-2 S-mediated barrier dysfunction. (Related to Figure 7). (A)** TEER assay of HPMEC treated with the indicated antibody and 10 µg/mL SARS-CoV-2 S. Data are control conditions from Figure 7C from n=2 biological replicates. **(B)** Same as A but treated with TGFBR inhibitor SB431542 (1 µM). Data are control conditions from Figure 7D from n=3 biological replicates. **(C)** Data are representative images from Figure 7E from n=3 biological replicates. **(D)** Data are representative images from Figure 7H from n=3 biological replicates. For all panels, sialic acid is stained in green and nuclei are stained with Hoechst in blue with scale bars at 100 µm. Dotted lines are the normalized untreated control conditions. All data are plotted as mean +/- SEM with ***p<0.001 by ANOVA with multiple comparisons.

Methods

EXPERIMENTAL MODELS AND SUBJECT DETAILS

Mice

Six- to eight-week-old wild-type C57BL/6J female mice were purchased from the Jackson Laboratory and housed at the University of California, Berkeley Animal Facility under specific pathogen-free conditions. Mice were housed in temperature-controlled environments on a 12-hour light and dark cycle, with food and water provided ad libitum. All experiments and procedures were pre-approved by the UC Berkeley Animal Care and Use Committee, Protocol AUP-2014-08-6638-2.

Cell Lines

HEK293T cells used for lentivirus production were obtained from ATCC and maintained in DMEM, high glucose, and GlutaMAX^{TM} (Gibco) supplemented with 10% FBS (Corning) and 1% penicillin/streptomycin (Gibco) (D10 medium) at 37°C with 5% CO_2. Calu-3 human lung epithelial cells were obtained from the UC Berkeley Cell Culture Facility and maintained in D10 medium at 37°C with 5% CO_2. Human pulmonary microvascular endothelial cells (HPMEC) [line HpMEC-ST1.6R] were a gift from Dr. J.C. Kirkpatrick at Johannes Gutenberg University, Germany. These cells were isolated from an adult human male donor, and an immortalized clone was selected that displayed all major phenotypic makers of pulmonary endothelial cells (65). HPMEC were cultured in endothelial cell growth basal medium 2 supplemented with an Endothelial Cell Growth Medium-2 (EGM-2^{TM}) supplemental bullet kit (Lonza). Cells were maintained at 37°C with 5% CO_2. This study produced several genetically modified versions of these parental cells, including HPMEC overexpressing the human ACE2 (hACE2) gene (HPMEC/ACE2) as well several knockout cell lines. The hACE2 encoding plasmid was a gift from Hyeryun Choe (Addgene plasmid #1786; http://n2t.net/addgene:1786; RRID:Addgene_1786) (66). Vero-E6 cells were used for SARS-CoV-2 titration and maintained in D10 media at 37°C with 5% CO_2.

Recombinant Proteins

Sequences encoding for full length, stabilized SARS-CoV-2 S ectodomain and RBD (based on the Wuhan-Hu-1 sequence) (67) were expressed and purified from stably transformed 293 cells, as previously reported (68). Purified proteins were formulated at ~1 mg/mL in PBS and stored in aliquots at -80° C. Recombinant DENV serotype 2 NS1 was purchased from the Native Antigen Company and characterized previously (Dengue virus serotype 2 NS1 [accession # P29990.1, Thailand/16681/84]) (35). SARS-CoV-2 S stabilized trimers from diverse viral variants were purchased from the Native Antigen Company including B.1.1.7 (Alpha variant, product #REC31924), B.1.351 (Beta variant, product #REC31963), B.1.1.28/P.1 (Gamma variant, product #REC31944), and B.1.617.2+AY.1+AY.2+AY.3 (Delta variant, product #REC31975). Recombinant VEGF (V7259) and TGF-β1 (100-21) was purchased from Sigma and PeproTech, respectively, and resuspended/stored in accordance with the manufacturer's instructions.

Vesicular Stomatitis Virus (VSV) Spike Pseudotype Virus Production and Infection

SARS-CoV-2 S pseudotyped virions were produced using the VSV-ΔG-rLuc system, originating from the VSV Indiana serotype full-length complementary DNA clone in which the G glycoprotein was exchanged for a *Renilla* Luciferase reporter gene. In brief, 15-cm^2 dishes of HEK293T cells

were transfected with a plasmid encoding SARS-CoV-2 S (Wuhan-Hu-1, Accession #QHD43416.1) using 45 µg total DNA. At 24 hours post-transfection, VSV-G expressing VSV-ΔG-rLuc pseudotyped virions were used to infect the transfected HEK293T cells. Medium was harvested 48 hours post-transfection and ultracentrifuged for 1.5 hours at 110,000 x g in a 20% sucrose cushion in NTE buffer (150 mM NaCl, 40 mM Tris-HCl, and 1 mM EDTA, pH 8.0). For viral resuspension, NTE Buffer was supplemented with 5% sucrose, and viral aliquots were stored at -80 °C.

SARS-CoV-2 Stock Production and Infection

Stocks of SARS-CoV-2 were produced as previously described (69). In brief, the USA-WA1/2020 strain of SARS-CoV-2 was obtained from BEI Resources and passed through a 0.45 µM syringe filter. Five µL of this filtered stock was added to T-175 flasks of Vero-E6 cells to produce virus passage 1. Cytopathic effect (CPE) was monitored daily and flasks were frozen down when ~70% cytopathic effect was evident (~48 hpi). Thawed lysates were then collected, and cell debris was pelleted at 3000 rpm for 20 min. Clarified viral supernatant was then aliquoted, and infectious virus was quantified by $TCID_{50}$. To produce passage 2, SARS-CoV-2 working stocks, 5 µL of the passage 1 stock was inoculated onto T175 flasks of Vero-E6 cells as described above. Viral titers obtained ranged from 1×10^6–5×10^6 $TCID_{50}$ units/mL.

METHOD DETAILS

Lentivirus Production and Transduction

Lentivirus particles encoding human ACE2 or CRISPR guide RNAs targeting the genes indicated in the figures were produced using a second-generation lentivirus system as reported previously (70). In brief, lentivirus vectors were transfected into 293T cells using a lipofectamine 3000 transfection protocol according to the manufacturer's instructions, along with a packaging vector (psPAX2) and a pseudotyping vector (pMD2.G). Medium was replaced on transfected cells 12 hours post-transfection. Lentivirus released into the medium of transfected cells was collected at 24-, 36-, and 48-hours post-transfection, and pooled lentivirus-containing media was filtered through a 0.45 µM syringe filter (Millipore). Target HPMEC were incubated with lentivirus for 48 hours and then selected with 2 µg/mL puromycin (Sigma) for 3 passages.

Trans-Epithelial/Endothelial Electrical Resistance Assay

Epithelial and endothelial barrier disruption (hyperpermeability) was measured through a Trans-Epithelial/Endothelial Electrical Resistance (TEER) Assay as previously described (35). In brief, $6x10^4$ HPMEC or $2x10^5$ Calu-3 were seeded in 300 µL into the apical chambers of 24-well transwell polycarbonate membrane inserts (Transwell permeable support, 0.4 µM, 6.5 mm insert; Corning) and 1.5 mL of medium was added to the basolateral chamber. Medium was changed daily from both the apical and basolateral chambers until cells formed a complete monolayer measured through maximal barrier resistance (~3 days for HPMEC and ~15 days for Calu-3). On the day of the experiment, TEER of each transwell was measured to ensure that cell resistance levels were at a minimum value and roughly equivalent (within 5 ohms). Transwells with outlier resistance values were excluded from the experiment. Treatments (indicated in the figures) were added to the apical chamber of the transwells. Electrical resistance values were measured in ohms (Ω) at the time-points indicated in the figures using an Epithelial Volt Ohm Meter (EVOM) with a "chopstick" electrode (World Precision Instruments). Inserts with untreated cells, as well as inserts with no cells containing medium alone (blank), were used as negative controls to calculate

the baseline electrical resistance. Relative TEER was calculated as a ratio of resistance values as (Ω experimental condition-Ω blank)/(Ω untreated cells-Ω blank).

Endothelial/Epithelial Glycocalyx Layer (EGL) Disruption Assays

To measure the capacity of protein treatments to mediate EGL disruption, $6x10^4$ HPMEC or $2x10^5$ Calu-3 cells were seeded on 0.2% gelatin- (Sigma) coated glass coverslips in 24-well plates. Cells were allowed to form a fully confluent monolayer over three days (HPMEC) or ~15 days (Calu-3), with medium changes every other day. On the day of the experiment, the treatments indicated in the figures were added directly to wells. Treatments and cells were allowed to incubate for the indicated times (generally 24 hours for S treatments) and then cells were washed twice with 1X PBS and fixed with 4% formaldehyde/PBS (Thermo Fisher Scientific). Coverslips were mounted onto microscope slides on a drop of ProLong Gold (Thermo Fisher Scientific) and imaged using a Zeiss LSM 710 inverted confocal microscope (CRL Molecular Imaging Center, UC Berkeley). EGL disruption was assessed by monitoring surface levels of sialic acid on the cell surface using the sialic acid-specific lectin, Wheat Germ Agglutinin (WGA) conjugated to Alexa Fluor 647 (Thermo Fisher Scientific, W32466), hyaluronic acid (Abcam ab53842), heparan sulfate (amsbio, clone F58-10E6, 370255-s), or chondroitin sulfate (Thermo Fisher Scientific, clone CS-56, ma1-83055). EGL disrupting enzyme expression were assessed on saponin permeabilized cells for hyaluronidase (Abcam, clone PH20, ab196596) and neuraminidase 2 (Thermo Fisher Scientific, pa5-35114). For staining, HPMEC were live cell stained at 100 µg/mL of WGA-647 diluted in the medium of live cells 1 hour pre-fixation. All other GAGs (HA, HS, CS) were stained on fixed cells with the coverslip turned onto a 15-µl drop of antibody containing staining buffer. Nuclei were stained by adding Hoechst 33342 (Immunochemistry) at a dilution of 1:200. All microscopy images were captured at 20x magnification.

***In Vivo* Dermal Vascular Leak Assay**

A murine dermal leak model was utilized to investigate vascular leak triggered by the S glycoprotein as previously described (35). In brief, the dorsal dermises of 6-7-week-old WT C57BL/6J female mice (purchased from Jackson Labs) were shaved. After 3-4 days, the indicated treatments (typically 10 µg of SARS-CoV-2 S) were injected intradermally (ID) into discrete spots in the shaved mouse dermis (50 µL/injection site). Immediately following ID injections, 150 µL of 10-kDa dextran conjugated to Alexa Fluor 680 (1 mg/mL; Sigma) was delivered intravenously (IV). Two hours post-injections, mice were euthanized, and the dorsal dermises were removed and placed in petri dishes. Fluorescence signal accumulation in the mouse dermises was visualized using a fluorescence scanner (LI-COR Odyssey CLx Imaging system) at a wavelength of 700 nm. Leakage was quantified around the injection sites using Image Studio software (LI-COR Biosciences). For small molecule inhibitor experiments, the inhibitor was mixed with SARS-CoV-2 S for 30 minutes before the ID injection.

***In Vivo* Systemic Leak**

To investigate systemic vascular leak triggered by SARS-CoV-2 S, we conducted a modified systemic vascular leak assay as described previously (30). In brief, 50 µg of SARS-CoV-2 S or OVA were administered to mice intranasally. Twenty-two hpt, mice received an IV injection of 10-kDa dextran conjugated to Alexa Fluor 680 (150 µL, 1 mg/mL; Sigma). This tracer dye was allowed to circulate in mice for 2 hours, at which time mice were euthanized and organs (lungs, spleen, liver, small intestine, and brain) were collected and placed on petri dishes. Fluorescence

34

signal accumulation in organs was visualized using a fluorescence scanner (LI-COR Odyssey CLx Imaging system) at a wavelength of 700 nm. Leakage was quantified using Image Studio software (LI-COR Biosciences).

EGL Enzyme Preparation and Digestion

To test for a contribution of glycan components to S-mediated endothelial dysfunction, recombinant enzymes were used to digest specific glycan components, including hyaluronic acid, heparan sulfate, sialic acid, and chondroitin sulfate. Recombinant heparin lyases I and III were obtained from IBEX and HPMEC were treated with 5 mU/mL of each, recombinant hyaluronidase (Sigma, H3506) was treated at 10 μg/mL, recombinant neuraminidase (Sigma, N2876) was treated at 1 U/mL, and recombinant chondriotinase ABC (Sigma, C3667) was treated at 25 mU/mL. All enzymes were added to HPMEC simultaneously with S and TEER/EGL assays were conducted 24 hpt as described above.

CRISPR-Cas9 Knockout

To produce gene-specific knockout cell lines, we utilized a CRISPR-Cas9 pipeline based on the lentiCRISPR v2 lentivirus construct obtained from Feng Zhang (Addgene plasmid # 52961; http://n2t.net/addgene:52961; RRID:Addgene_52961), as previously described (71). In brief, guide RNA targeting sequences were selected from the Brunello CRISPR KO guide library (72) and cloned into the lentiCRISPR v2 plasmid. Guide RNA sequences utilized in this study are summarized in **Table S3**. Lentivirus was produced as described above, and HPMEC were transduced and selected in EGM-2 medium containing 2 μg/mL of puromycin and passaged three times in selection. Polyclonal populations of cells were characterized for functional knockout through either a western blot to measure protein expression or through HS staining by IFA to confirm function (for HS biosynthetic pathway genes).

RNA Sequencing

To characterize the transcriptional response of cells treated with SARS-CoV-2 S, we conducted RNA-Sequencing. In brief, HPMEC and HPMEC/ACE2 were treated with 10 μg/mL SARS-CoV-2 S, and cell lysates were collected in TRI reagent (Sigma) 24 hours post-treatment. Total RNA was extracted using a Direct-zol RNA miniprep kit (Zymo Research) per the manufacturer's instructions. RNA was quantified using a Qubit Flex Fluorometer (ThermoFisher), and quality was measured by Bioanalyzer (RNA Pico; Agilent). 1 μg of RNA was used for library preparation with the SMARTer Stranded Total RNA Sample Prep Kit - HI Mammalian (Takara Bio), following the manufacturer's instructions. Quality of prepared libraries was evaluated by Bioanalyzer (High Sensitivity DNA; Agilent) and sequenced on the NovaSeq 6000 (Illumina) using S4 flow cell and 150-base pair paired-end sequencing at the UCSF Center for Advanced Technology. Following sequencing of sample libraries, quality control was performed on the fastq files to ensure that sequencing reads met preestablished cutoffs for number of reads and quality using FastQC (version 0.11.8) (73) and MultiQC (version 1.8) (74). Quality filtering and adapter trimming were performed using BBduk tools (version 38.76, https://sourceforge.net/projects/bbmap). Remaining reads were aligned to the ENSEMBL GRCh38 human reference genome assembly (release 33) using STAR (version 2.7.0f) (75), and gene frequencies were counted using featureCounts (version 2.0.0) within the Subread package (76). Comparative analysis of DEGs was performed using a negative binomial distribution model used by DESeq2 (version 1.28.1) (77) as implemented in R (version 4.0.3). All genes passing a Benjamini-Hochberg (BH)-adjusted P value

threshold of 0.05 were included. Hierarchical clustering of DEGs and visualization were performed using the ComplexHeatmap (version 2.4.2) and pheatmap package (version 1.0.12). The clustering method used is complete linkage, and clusters are based on Euclidean distance. Identified DEGs were analyzed by STRING to identify predicted protein-protein interaction networks as well as enriched pathway analysis (https://string-db.org/).

TGF-β Enzyme Linked Immunosorbent Assay (ELISA)

To measure levels of TGF-β1 in the supernatants of S-treated cells, we used the Human TGF-beta 1 DuoSet ELISA (DY240, R&D Systems). In brief, cell supernatants were collected 24 h after treatment with SARS-CoV-2 S and activated with 1N HCl in order to detect immunoreactive TGF-β1. After pH neutralization, samples and recombinant TGF-β1 standards were transferred to ELISA plates coated with mouse anti-human TGF-β1 capture antibody and incubated for 2 h at room temperature. Afterwards, plates were incubated with biotinylated chicken anti-human TGF-β1 detection antibody and then with streptavidin-horseradish peroxidase (HRP) for signal detection with tetramethylbenzidine (TMB) substrate. The optical density of each well was determined using a microplate reader set to 450 nm. TGF-β1 levels were determined by interpolation from four-parameter logistic (4-PL) standard curves.

Size-exclusion Chromatography with Multi-Angle Light Scattering (SEC-MALS)

To characterize the purity and oligomeric state of soluble SARS-CoV-2 S and RBD, purified proteins were injected onto a SRT SEC-1000 column (4.6x300 mm, Sepax) at 0.35 mL/min in PBS (for S) or a Superdex 200 Increase column (3.2x300 mm, Cytiva) at 0.15 mL/min in PBS (for RBD). The column and the entire SEC-MALS system, which includes a 1260 Infinity II HPLC (Agilent), a miniDAWN TREOS II MALS detector (Wyatt) and a Optilab T-rEX refractive index detector (Wyatt), were equilibrated in PBS for at least 24 h prior to analysis. Molecular weights of S and RBD were determined using Astra (Wyatt).

Small Molecule Inhibitors, Peptides, and Antibodies

The following small molecule inhibitors and antibodies were used for TEER and EGL inhibition assays: ATN-161 (Sigma, SML2079), SB 431542 hydrate (Sigma, S4317), heparin (Sigma, H3393), anti-Spike (Genetex, 1A9, GTX632604), anti-Spike (Absolute Antibody, CR3022), rabbit anti-TGFBR1 (Thermo Fisher Scientific, PA5-32631). All chemicals and antibodies were resuspended and utilized per the manufacturer's instructions. The RGD, KGD, and DRG peptides were synthesized by Sigma.

SDS-PAGE and Western Blot

Recombinant proteins or cell lysates were collected in protein sample buffer (0.1 M Tris pH 6.8, 4% SDS, 4 mM EDTA, 286 mM 2-mercaptoethanol, 3.2 M glycerol, 0.05% bromophenol blue) and resolved by SDS-PAGE. Proteins were then transferred to nitrocellulose membranes and probed with primary antibodies diluted in PBS with 0.1% Tween20 (PBST) containing 5% skim milk. Membranes and antibodies were incubated overnight rocking at 4°C. The next day, membranes were washed three times with PBST before being probed with HRP-conjugated secondary antibodies diluted at 1:5,000 in 5% milk in PBST at room temperature for 1 hour. Membranes were then washed with PBST three more times before being developed with homemade ECL reagents and imaged on a ChemiDoc system with Image Lab software (Bio-

Rad). The following antibodies were used in this study: goat anti-ACE2 (R&D Systems, AF933), rabbit anti-integrin alpha 5 (Abcam, ab150361), rabbit anti-ITGB1 (Thermo Fisher Scientific, PA5-29606), rabbit anti-Heparanase 1 (Abcam, EPR22365-230, ab254254), rabbit anti-MMP-9 (Cell Signaling Technology, #3852), mouse anti-TACE/ADAM17 (Santa Cruz Biotechnologies, B-6, sc-390859), mouse anti-Cathepsin L (Thermo Fisher Scientific, 33-2, BMS1032), rabbit anti-TGFBR1 (Thermo Fisher Scientific, PA5-32631), mouse anti-His (MA1-21315, Thermo Scientific), mouse anti-β-actin HRP (Santa Cruz Biotechnologies, sc-47778 HRP), goat anti-mouse HRP (Biolegend, 405306), donkey anti-rabbit HRP (Biolegend, 406401), donkey anti-human HRP, Biolegend, 410902).

Statistics

All data were plotted and quantitative analyses performed using GraphPad Prism 8 software. Experiments were repeated at least 3 times, except when indicated otherwise. Experiments were designed and performed with both positive and negative controls, which were used for inclusion/exclusion determination. Researchers were not blinded during experiments. For immunofluorescence microscopy experiments, images of random fields were captured. For all experiments with quantitative analyses, data are displayed as mean ± SEM, except for TEER quantification, which displays mean ± SD. Statistical tests used in this study include ANOVA analysis with multiple comparisons test as well as t-tests, as indicated in the figures. Resultant p-values from the above statistical tests are displayed as n.s., not significant $p > 0.05$; *$p < 0.05$; **$p < 0.01$; ***$p < 0.001$. All statistics not indicated are not significant.

Table S1: Table of all DEGs identified by RNA-seq for HPMEC. logFC is log2 fold change between S-treated and untreated HPMEC; lfcSE is standard error of logFC measurement; padj is the Benjamini-Hochberg adjusted p-value. DEGs sorted by padj in ascending order.

	logFC	lfcSE	padj
TGFBI	1.371118	0.079699	3.56E-62
FN1	0.953106	0.066069	2.54E-43
VCAN	0.952346	0.087644	7.96E-24
COL5A1	1.26353	0.124811	1.55E-20
POSTN	1.383791	0.154461	9.37E-16
TAGLN	1.961064	0.226242	1.05E-14
THBS1	0.63853	0.073949	1.20E-14
BGN	0.647704	0.077844	1.56E-13
TTN	-0.90536	0.109385	2.01E-13
FBLN5	2.729718	0.334751	5.01E-13
COL4A2	0.773955	0.10208	4.42E-11
SPOCK1	1.286272	0.170702	5.80E-11
CCDC80	0.739803	0.098474	6.36E-11
ITGA4	0.594026	0.08376	1.35E-09
LTBP2	0.679898	0.098004	3.80E-09
EFEMP1	0.475991	0.069675	7.50E-09
COL4A1	0.817672	0.135217	1.24E-06
SERPINE1	0.409463	0.069775	3.49E-06
SCG2	-0.60211	0.103482	4.46E-06
GREM1	0.654721	0.117933	2.02E-05
COL1A1	0.431159	0.078372	2.56E-05
NNMT	0.600157	0.111027	4.20E-05
AEBP1	0.930373	0.176007	7.76E-05
PRRG2	8.333765	1.641456	0.000228
CTGF	0.398347	0.081507	0.000569
DPP4	-0.48372	0.099028	0.000569
PDGFA	1.273166	0.261147	0.000575
IGFBP5	0.706101	0.145405	0.000611
MARCKSL1	0.701964	0.145904	0.000739
SFRP1	-0.38668	0.081889	0.001112
TUBB3	0.6127	0.13006	0.001136
MX1	-0.76726	0.163872	0.001267
LIPG	0.612031	0.134572	0.002311
CYR61	0.366945	0.080743	0.002311
IGFBP7	0.464181	0.104312	0.003505
IFIT1	-0.55868	0.127617	0.004756
OAS1	-0.79358	0.183505	0.005898
PDPN	0.483369	0.112926	0.00701
CALR	0.325416	0.076226	0.007127

SRPX2	0.446491	0.10468	0.007127
OAS3	-0.51575	0.122883	0.009417
OAS2	-0.66492	0.162087	0.013912
PAG1	-0.71465	0.174574	0.0141
VN1R1	6.9542	1.701353	0.014154
CALU	0.41333	0.102276	0.016868
KRT7	0.338055	0.084121	0.01817
HYOU1	0.412395	0.102844	0.018456
LRRC16B	7.396787	1.854452	0.019768
XYLT2	0.503855	0.126489	0.019799
TNFRSF1B	-0.91591	0.230701	0.020517
COL4A5	-0.37191	0.093873	0.02083
ITGB5	0.361329	0.09158	0.021868
SOCS3	1.176033	0.301821	0.025852
FLVCR2	-0.53739	0.13793	0.025852
FAP	1.371427	0.357547	0.032514
ATP2B4	-0.34275	0.089574	0.033158
NOVA1	-1.09926	0.28812	0.034076
CAPN2	-0.38218	0.1007	0.035531
VEGFA	0.511021	0.134666	0.035531
CD82	-0.56799	0.149776	0.035531
GDI1	0.416437	0.110753	0.039769
ENDOD1	-0.37823	0.100823	0.040494
IGF1	-7.02501	1.881955	0.042918
CD177	-7.16087	1.922983	0.043724
GALNT2	0.416722	0.112014	0.043724

Table S2: Table of all DEGs identified by RNA-seq for HPMEC/ACE2. logFC is log2 fold change between S-treated and untreated HPMEC; lfcSE is standard error of logFC measurement; padj is the Benjamini-Hochberg adjusted p-value. DEGs sorted by padj in ascending order.

	logFC	lfcSE	padj
FN1	1.155469	0.084239	1.11E-38
VCAN	1.365061	0.10998	1.55E-31
TGFBI	1.170262	0.104192	1.31E-25
ARNT2	20.72869	2.82404	5.88E-10
THBS1	0.677006	0.091917	5.88E-10
LTBP2	0.700158	0.105644	7.83E-08
FBLN5	3.224537	0.498445	1.94E-07
COL4A2	0.849703	0.132168	2.21E-07
TTN	-0.86289	0.137856	5.91E-07
TAGLN	2.00945	0.330354	1.63E-06
POSTN	1.694383	0.281304	2.14E-06
COL4A1	1.188305	0.198676	2.54E-06
TUBA1A	0.843212	0.14226	3.26E-06
COL5A1	0.965757	0.168631	1.00E-05
MSN	0.387547	0.073553	0.000126
SCG2	-0.6782	0.132551	0.000268
CALU	0.527747	0.103945	0.00031
CCDC80	0.590436	0.11718	0.000358
COL1A1	0.525848	0.104801	0.000379
SPOCK1	1.138718	0.231532	0.000599
HYOU1	0.511391	0.104165	0.000599
IGFBP7	0.679211	0.141543	0.000999
ACE2	0.49024	0.103388	0.001268
POPDC2	8.229141	1.764277	0.001776
ITGB5	0.646374	0.138927	0.001804
SERPINE1	0.365501	0.080207	0.002747
BGN	0.757858	0.16736	0.003031
FLNC	-0.47501	0.105658	0.003409
SERPINE2	0.818751	0.183007	0.003646
SCRG1	8.387214	1.960532	0.008651
PCDHGC4	4.979312	1.168255	0.008989
TIAM1	-7.87209	1.861754	0.010127
KLF15	7.792539	1.914317	0.019003
FAT3	-7.76917	1.908722	0.019003
C9orf163	7.877015	1.940926	0.019433
ITGA4	0.58027	0.145971	0.02688
EFEMP1	0.442293	0.112161	0.02948
RPL26	-0.566	0.143645	0.02948
RUNX1T1	-5.25768	1.340464	0.030956

PDPN	0.762492	0.194708	0.03097
HTRA1	0.42207	0.110751	0.046464

Table S3: Primers used to clone guide RNA sequences into the lentiCRISPR v2 plasmid**.**

Target	Guide RNA Sequence
gRNA_NTG_1_F	CACCGTACTAACGCCGCTCCTACAG
gRNA_NTG_1_R	AAACCTGTAGGAGCGGCGTTAGTAC
gRNA_NTG_2_F	CACCGGATCCAGGAGTGATCGAGTA
gRNA_NTG_2_R	AAACTACTCGATCACTCCTGGATCC
gRNA_ACE2_59272_1_F	CACCGAACATCTTCATGCCTATGTG
gRNA_ACE2_59272_1_R	AAACCACATAGGCATGAAGATGTTC
gRNA_ACE2_59272_2_F	CACCGCAGGATCCTTATGTGCACAA
gRNA_ACE2_59272_2_R	AAACTTGTGCACATAAGGATCCTGC
gRNA_CTSL_1514_1_F	CACCGAGATGTTCCGGAAAACTGGG
gRNA_CTSL_1514_1_R	AAACCCCAGTTTTCCGGAACATCTC
gRNA_CTSL_1514_2_F	CACCGCAGTATGTTCAGGATAATGG
gRNA_CTSL_1514_2_R	AAACCCATTATCCTGAACATACTGC
gRNA_HPSE_10855_1_F	CACCGTAAAAATGTCCAATACATCA
gRNA_HPSE_10855_1_R	AAACTGATGTATTGGACATTTTTAC
gRNA_HPSE_10855_2_F	CACCGTGGCAATCTCAAGTCAACCA
gRNA_HPSE_10855_2_R	AAACTGGTTGACTTGAGATTGCCAC
gRNA_TGFBR1_7046_1_F	CACCGAGAACGTTCGTGGTTCCGTG
gRNA_TGFBR1_7046_1_R	AAACCACGGAACCACGAACGTTCTC
gRNA_TGFBR1_7046_2_F	CACCGATGGGCAAGACCGCTCGCCG
gRNA_TGFBR1_7046_2_R	AAACCGGCGAGCGGTCTTGCCCATC
gRNA_ADAM17_6868_1_F	CACCGAATCAGAATCAACACAGATG
gRNA_ADAM17_6868_1_R	AAACCATCTGTGTTGATTCTGATTC
gRNA_ADAM17_6868_2_F	CACCGACAAAATTTCAAGGTCGTGG
gRNA_ADAM17_6868_2_R	AAACCCACGACCTTGAAATTTTGTC
gRNA_IL6R_3570_1_F	CACCGCCGTGGCCAGAAACCCCCGC
gRNA_IL6R_3570_1_R	AAACGCGGGGGTTTCTGGCCACGGC
gRNA_IL6R_3570_2_F	CACCGTGGAAACTATTCATGCTACC
gRNA_IL6R_3570_2_R	AAACGGTAGCATGAATAGTTTCCAC
gRNA_MMP9_4318_1_F	CACCGACTACTCGGAAGACTTGCCG
gRNA_MMP9_4318_1_R	AAACCGGCAAGTCTTCCGAGTAGTC
gRNA_MMP9_4318_2_F	CACCGCCGCTATGGTTACACTCGGG
gRNA_MMP9_4318_2_R	AAACCCCGAGTGTAACCATAGCGGC
gRNA_XYLT2_64132_1_F	CACCGAGGACACAGACAGTTCAGCA
gRNA_XYLT2_64132_1_R	AAACTGCTGAACTGTCTGTGTCCTC
gRNA_XYLT2_64132_2_F	CACCGCCAGGGCTATGATAACGTGC
gRNA_XYLT2_64132_2_R	AAACGCACGTTATCATAGCCCTGGC
gRNA_SLC35B2_347734_1_F	CACCGCAGGTGTCTTATCTGACTTG

gRNA_SLC35B2_347734_1_R	AAACCAAGTCAGATAAGACACCTGC
gRNA_SLC35B2_347734_2_F	CACCGCTGGGTCCATGACTCCGGAG
gRNA_SLC35B2_347734_2_R	AAACCTCCGGAGTCATGGACCCAGC
gRNA_ITGA5_3678_1_F	CACCGCCCCGAGTACCTGATCAACC
gRNA_ITGA5_3678_1_R	AAACGGTTGATCAGGTACTCGGGGC
gRNA_ITGA5_3678_2_F	CACCGTGGATCGGACCCCTGACGGG
gRNA_ITGA5_3678_2_R	AAACCCCGTCAGGGGTCCGATCCAC
gRNA_ITGB1_3688_1_F	CACCGAATGTAACCAACCGTAGCAA
gRNA_ITGB1_3688_1_R	AAACTTGCTACGGTTGGTTACATTC
gRNA_ITGB1_3688_2_F	CACCGGAACGGGGTGAATGGAACAG
gRNA_ITGB1_3688_2_R	AAACCTGTTCCATTCACCCCGTTCC

References

1.   Xu Z, Shi L, Wang Y, Zhang J, Huang L, Zhang C, et al. Pathological findings of COVID-19 associated with acute respiratory distress syndrome. Lancet Respir Med. 2020;8(4):420-2.

2.   Zhang B, Zhou X, Qiu Y, Song Y, Feng F, Feng J, et al. Clinical characteristics of 82 cases of death from COVID-19. PLoS One. 2020;15(7):e0235458.

3.   Yang X, Yu Y, Xu J, Shu H, Xia J, Liu H, et al. Clinical course and outcomes of critically ill patients with SARS-CoV-2 pneumonia in Wuhan, China: a single-centered, retrospective, observational study. Lancet Respir Med. 2020;8(5):475-81.

4.   Zhu N, Zhang D, Wang W, Li X, Yang B, Song J, et al. A Novel Coronavirus from Patients with Pneumonia in China, 2019. N Engl J Med. 2020;382(8):727-33.

5.   Jin Y, Ji W, Yang H, Chen S, Zhang W, Duan G. Endothelial activation and dysfunction in COVID-19: from basic mechanisms to potential therapeutic approaches. Signal Transduct Target Ther. 2020;5(1):293.

6.   Bonaventura A, Vecchié A, Dagna L, Martinod K, Dixon DL, Van Tassell BW, et al. Endothelial dysfunction and immunothrombosis as key pathogenic mechanisms in COVID-19. Nat Rev Immunol. 2021;21(5):319-29.

7.   Hartenian E, Nandakumar D, Lari A, Ly M, Tucker JM, Glaunsinger BA. The molecular virology of coronaviruses. J Biol Chem. 2020;295(37):12910-34.

8.   Kim D, Lee JY, Yang JS, Kim JW, Kim VN, Chang H. The Architecture of SARS-CoV-2 Transcriptome. Cell. 2020;181(4):914-21.e10.

9.   Letko M, Marzi A, Munster V. Functional assessment of cell entry and receptor usage for SARS-CoV-2 and other lineage B betacoronaviruses. Nat Microbiol. 2020;5(4):562-9.

10.   Hoffmann M, Kleine-Weber H, Schroeder S, Krüger N, Herrler T, Erichsen S, et al. SARS-CoV-2 Cell Entry Depends on ACE2 and TMPRSS2 and Is Blocked by a Clinically Proven Protease Inhibitor. Cell. 2020;181(2):271-80.e8.

11.   Li F. Structure, Function, and Evolution of Coronavirus Spike Proteins. Annu Rev Virol. 2016;3(1):237-61.

12.   Andersen KG, Rambaut A, Lipkin WI, Holmes EC, Garry RF. The proximal origin of SARS-CoV-2. Nat Med. 2020;26(4):450-2.

13.   Hoffmann M, Kleine-Weber H, Pöhlmann S. A Multibasic Cleavage Site in the Spike Protein of SARS-CoV-2 Is Essential for Infection of Human Lung Cells. Mol Cell. 2020;78(4):779-84.e5.

14.   Hoffmann M, Hofmann-Winkler H, Smith JC, Krüger N, Sørensen LK, Søgaard OS, et al. Camostat mesylate inhibits SARS-CoV-2 activation by TMPRSS2-related proteases and its metabolite GBPA exerts antiviral activity. bioRxiv. 2020.

15.   Koch J, Uckeley ZM, Doldan P, Stanifer M, Boulant S, Lozach P-Y. Host Cell Proteases Drive Early or Late SARS-CoV-2 Penetration. bioRxiv. 2020:2020.12.22.423906.

16.   Letarov AV, Babenko VV, Kulikov EE. Free SARS-CoV-2 Spike Protein S1 Particles May Play a Role in the Pathogenesis of COVID-19 Infection. Biochemistry (Mosc). 2021;86(3):257-61.

17.   Zhang L, Jackson CB, Mou H, Ojha A, Peng H, Quinlan BD, et al. SARS-CoV-2 spike-protein D614G mutation increases virion spike density and infectivity. Nat Commun. 2020;11(1):6013.

18.   Park EJ, Myint PK, Appiah MG, Darkwah S, Caidengbate S, Ito A, et al. The Spike Glycoprotein of SARS-CoV-2 Binds to β1 Integrins Expressed on the Surface of Lung Epithelial Cells. Viruses. 2021;13(4).

19.   Sigrist CJ, Bridge A, Le Mercier P. A potential role for integrins in host cell entry by SARS-CoV-2. Antiviral Res. 2020;177:104759.

20.   Clausen TM, Sandoval DR, Spliid CB, Pihl J, Perrett HR, Painter CD, et al. SARS-CoV-2 Infection Depends on Cellular Heparan Sulfate and ACE2. Cell. 2020;183(4):1043-57.e15.

21.   Kuba K, Imai Y, Rao S, Gao H, Guo F, Guan B, et al. A crucial role of angiotensin converting enzyme 2 (ACE2) in SARS coronavirus-induced lung injury. Nat Med. 2005;11(8):875-9.

22.   Wu Z, Wang Z, Dai F, Liu H, Ren W, Chang J, et al. Dephosphorylation of Y685-VE-Cadherin Involved in Pulmonary Microvascular Endothelial Barrier Injury Induced by Angiotensin II. Mediators Inflamm. 2016;2016:8696481.

23.   Haga S, Yamamoto N, Nakai-Murakami C, Osawa Y, Tokunaga K, Sata T, et al. Modulation of TNF-alpha-converting enzyme by the spike protein of SARS-CoV and ACE2 induces TNF-alpha production and facilitates viral entry. Proc Natl Acad Sci U S A. 2008;105(22):7809-14.

24.   Colunga Biancatelli RML, Solopov PA, Sharlow ER, Lazo JS, Marik PE, Catravas JD. The SARS-CoV-2 spike protein subunit S1 induces COVID-19-like acute lung injury in K18-hACE2 transgenic mice and barrier dysfunction in human endothelial cells. American Journal of Physiology-Lung Cellular and Molecular Physiology. 2021;321(2):L477-L84.

25.   Lei Y, Zhang J, Schiavon CR, He M, Chen L, Shen H, et al. SARS-CoV-2 Spike Protein Impairs Endothelial Function via Downregulation of ACE 2. Circ Res. 2021;128(9):1323-6.

26.   Rysz S, Al-Saadi J, Sjöström A, Farm M, Campoccia Jalde F, Plattén M, et al. COVID-19 pathophysiology may be driven by an imbalance in the renin-angiotensin-aldosterone system. Nat Commun. 2021;12(1):2417.

27.   Beatty PR, Puerta-Guardo H, Killingbeck SS, Glasner DR, Hopkins K, Harris E. Dengue virus NS1 triggers endothelial permeability and vascular leak that is prevented by NS1 vaccination. Sci Transl Med. 2015;7(304):304ra141.

28.   Puerta-Guardo H, Glasner DR, Harris E. Dengue Virus NS1 Disrupts the Endothelial Glycocalyx, Leading to Hyperpermeability. PLoS Pathog. 2016;12(7):e1005738.

29.   Glasner DR, Ratnasiri K, Puerta-Guardo H, Espinosa DA, Beatty PR, Harris E. Dengue virus NS1 cytokine-independent vascular leak is dependent on endothelial glycocalyx components. PLoS Pathog. 2017;13(11):e1006673.

30.   Puerta-Guardo H, Glasner DR, Espinosa DA, Biering SB, Patana M, Ratnasiri K, et al. Flavivirus NS1 Triggers Tissue-Specific Vascular Endothelial Dysfunction Reflecting Disease Tropism. Cell Rep. 2019;26(6):1598-613.e8.

31.   Wang C, Puerta-Guardo H, Biering SB, Glasner DR, Tran EB, Patana M, et al. Endocytosis of flavivirus NS1 is required for NS1-mediated endothelial hyperpermeability and is abolished by a single N-glycosylation site mutation. PLoS Pathog. 2019;15(7):e1007938.

32.   Glasner DR, Puerta-Guardo H, Beatty PR, Harris E. The Good, the Bad, and the Shocking: The Multiple Roles of Dengue Virus Nonstructural Protein 1 in Protection and Pathogenesis. Annu Rev Virol. 2018.

33.   Glasner DR, Puerta-Guardo H, Beatty PR, Harris E. The Good, the Bad, and the Shocking: The Multiple Roles of Dengue Virus Nonstructural Protein 1 in Protection and Pathogenesis. Annu Rev Virol. 2018;5(1):227-53.

34.   Rodrigues SF, Granger DN. Blood cells and endothelial barrier function. Tissue Barriers. 2015;3(1-2):e978720.

35.   Biering SB, Akey DL, Wong MP, Brown WC, Lo NTN, Puerta-Guardo H, et al. Structural basis for antibody inhibition of flavivirus NS1-triggered endothelial dysfunction. Science. 2021;371(6525):194-200.

36.   Wan Y, Shang J, Graham R, Baric RS, Li F. Receptor Recognition by the Novel Coronavirus from Wuhan: an Analysis Based on Decade-Long Structural Studies of SARS Coronavirus. J Virol. 2020;94(7).

37.   Zhang Q, Chen CZ, Swaroop M, Xu M, Wang L, Lee J, et al. Heparan sulfate assists SARS-CoV-2 in cell entry and can be targeted by approved drugs in vitro. Cell Discov. 2020;6(1):80.

38.   Sarrazin S, Lamanna WC, Esko JD. Heparan sulfate proteoglycans. Cold Spring Harb Perspect Biol. 2011;3(7).

39.   Cuellar K, Chuong H, Hubbell SM, Hinsdale ME. Biosynthesis of chondroitin and heparan sulfate in chinese hamster ovary cells depends on xylosyltransferase II. J Biol Chem. 2007;282(8):5195-200.

40.   Kamiyama S, Suda T, Ueda R, Suzuki M, Okubo R, Kikuchi N, et al. Molecular cloning and identification of 3'-phosphoadenosine 5'-phosphosulfate transporter. J Biol Chem. 2003;278(28):25958-63.

41.   Hui L, Nie Y, Li S, Guo M, Yang W, Huang R, et al. Matrix metalloproteinase 9 facilitates Zika virus invasion of the testis by modulating the integrity of the blood-testis barrier. PLoS Pathog. 2020;16(4):e1008509.

42.   Pan P, Li G, Shen M, Yu Z, Ge W, Lao Z, et al. DENV NS1 and MMP-9 cooperate to induce vascular leakage by altering endothelial cell adhesion and tight junction. PLoS Pathog. 2021;17(7):e1008603.

43.   Kobayashi T, Kim H, Liu X, Sugiura H, Kohyama T, Fang Q, et al. Matrix metalloproteinase-9 activates TGF-β and stimulates fibroblast contraction of collagen gels. Am J Physiol Lung Cell Mol Physiol. 2014;306(11):L1006-15.

44.   Malapeira J, Esselens C, Bech-Serra JJ, Canals F, Arribas J. ADAM17 (TACE) regulates TGFβ signaling through the cleavage of vasorin. Oncogene. 2011;30(16):1912-22.

45.   Patra T, Meyer K, Geerling L, Isbell TS, Hoft DF, Brien J, et al. SARS-CoV-2 spike protein promotes IL-6 trans-signaling by activation of angiotensin II receptor signaling in epithelial cells. PLoS Pathog. 2020;16(12):e1009128.

46.   Etwebi Z, Landesberg G, Preston K, Eguchi S, Scalia R. Mechanistic Role of the Calcium-Dependent Protease Calpain in the Endothelial Dysfunction Induced by MPO (Myeloperoxidase). Hypertension. 2018;71(4):761-70.

47.   Goumans MJ, Liu Z, ten Dijke P. TGF-beta signaling in vascular biology and dysfunction. Cell Res. 2009;19(1):116-27.

48.   Wu C. Focal adhesion: a focal point in current cell biology and molecular medicine. Cell Adh Migr. 2007;1(1):13-8.

49.   Kechagia JZ, Ivaska J, Roca-Cusachs P. Integrins as biomechanical sensors of the microenvironment. Nat Rev Mol Cell Biol. 2019;20(8):457-73.

50.   Wipff PJ, Hinz B. Integrins and the activation of latent transforming growth factor beta1 - an intimate relationship. Eur J Cell Biol. 2008;87(8-9):601-15.

51.   Ruoslahti E, Pierschbacher MD. Arg-Gly-Asp: a versatile cell recognition signal. Cell. 1986;44(4):517-8.

52.   Ruoslahti E. RGD and other recognition sequences for integrins. Annu Rev Cell Dev Biol. 1996;12:697-715.

53.   Wang H, Radjendirane V, Wary KK, Chakrabarty S. Transforming growth factor beta regulates cell-cell adhesion through extracellular matrix remodeling and activation of focal adhesion kinase in human colon carcinoma Moser cells. Oncogene. 2004;23(32):5558-61.

54.   George S, Pal AC, Gagnon J, Timalsina S, Singh P, Vydyam P, et al. Evidence for SARS-CoV-2 Spike Protein in the Urine of COVID-19 Patients. Kidney360. 2021;2(6):924.

55.   Avolio E, Carrabba M, Milligan R, Kavanagh Williamson M, Beltrami A, Gupta K, et al. The SARS-CoV-2 Spike protein disrupts human cardiac pericytes function through CD147-receptor-mediated signalling: a potential non-infective mechanism of COVID-19 microvascular disease. Clin Sci (Lond). 2021.

56.   Beddingfield BJ, Iwanaga N, Chapagain PP, Zheng W, Roy CJ, Hu TY, et al. The Integrin Binding Peptide, ATN-161, as a Novel Therapy for SARS-CoV-2 Infection. JACC Basic Transl Sci. 2021;6(1):1-8.

57.   Ferreira-Gomes M, Kruglov A, Durek P, Heinrich F, Tizian C, Heinz GA, et al. SARS-CoV-2 in severe COVID-19 induces a TGF-β-dominated chronic immune response that does not target itself. Nat Commun. 2021;12(1):1961.

58.   Witkowski M, Tizian C, Ferreira-Gomes M, Niemeyer D, Jones TC, Heinrich F, et al. Untimely TGFβ responses in COVID-19 limit antiviral functions of NK cells. Nature. 2021.

59.   Modhiran N, Watterson D, Muller DA, Panetta AK, Sester DP, Liu L, et al. Dengue virus NS1 protein activates cells via Toll-like receptor 4 and disrupts endothelial cell monolayer integrity. Sci Transl Med. 2015;7(304):304ra142.

60.   Wessel AW, Dowd KA, Biering SB, Zhang P, Edeling MA, Nelson CA, et al. Levels of circulating NS1 impact West Nile virus spread to the brain. J Virol. 2021:JVI0084421.

61.   Biering SB, Sarnik SA, Wang E, Zengel JR, Sathyan V, Nguyenla X, et al. Genome-wide, bidirectional CRISPR screens identify mucins as critical host factors modulating SARS-CoV-2 infection. bioRxiv. 2021:2021.04.22.440848.

62.   Rebendenne A, Roy P, Bonaventure B, Chaves Valadão AL, Desmarets L, Rouillé Y, et al. Bidirectional genome-wide CRISPR screens reveal host factors regulating SARS-CoV-2, MERS-CoV and seasonal coronaviruses. bioRxiv. 2021:2021.05.19.444823.

63.   Ogata AF, Cheng CA, Desjardins M, Senussi Y, Sherman AC, Powell M, et al. Circulating SARS-CoV-2 Vaccine Antigen Detected in the Plasma of mRNA-1273 Vaccine Recipients. Clin Infect Dis. 2021.

64.   Modhiran N, Song H, Liu L, Bletchly C, Brillault L, Amarilla AA, et al. A broadly protective antibody that targets the flavivirus NS1 protein. Science. 2021;371(6525):190-4.

65.   Krump-Konvalinkova V, Bittinger F, Unger RE, Peters K, Lehr HA, Kirkpatrick CJ. Generation of human pulmonary microvascular endothelial cell lines. Lab Invest. 2001;81(12):1717-27.

66.   Li W, Moore MJ, Vasilieva N, Sui J, Wong SK, Berne MA, et al. Angiotensin-converting enzyme 2 is a functional receptor for the SARS coronavirus. Nature. 2003;426(6965):450-4.

67.   Amanat F, Stadlbauer D, Strohmeier S, Nguyen THO, Chromikova V, McMahon M, et al. A serological assay to detect SARS-CoV-2 seroconversion in humans. Nat Med. 2020;26(7):1033-6.

68.   Byrum JR, Waltari E, Janson O, Guo SM, Folkesson J, Chhun BB, et al. multiSero: open multiplex-ELISA platform for analyzing antibody responses to SARS-CoV-2 infection. medRxiv. 2021.

69.   Biering SB, Van Dis E, Wehri E, Yamashiro LH, Nguyenla X, Dugast-Darzacq C, et al. Screening a library of FDA-approved and bioactive compounds for antiviral activity against SARS-CoV-2. bioRxiv. 2020:2020.12.30.424862.

70.   Biering SB, Choi J, Halstrom RA, Brown HM, Beatty WL, Lee S, et al. Viral Replication Complexes Are Targeted by LC3-Guided Interferon-Inducible GTPases. Cell Host Microbe. 2017;22(1):74-85.e7.

71.   Sanjana NE, Shalem O, Zhang F. Improved vectors and genome-wide libraries for CRISPR screening. Nat Methods. 2014;11(8):783-4.

72.   Doench JG, Fusi N, Sullender M, Hegde M, Vaimberg EW, Donovan KF, et al. Optimized sgRNA design to maximize activity and minimize off-target effects of CRISPR-Cas9. Nat Biotechnol. 2016;34(2):184-91.

73.   Wingett SW, Andrews S. FastQ Screen: A tool for multi-genome mapping and quality control. F1000Res. 2018;7:1338.

74.   Ewels P, Magnusson M, Lundin S, Käller M. MultiQC: summarize analysis results for multiple tools and samples in a single report. Bioinformatics. 2016;32(19):3047-8.

75.   Dobin A, Gingeras TR. Mapping RNA-seq Reads with STAR. Curr Protoc Bioinformatics. 2015;51:11.4.1-.4.9.

76.   Liao Y, Smyth GK, Shi W. featureCounts: an efficient general purpose program for assigning sequence reads to genomic features. Bioinformatics. 2014;30(7):923-30.

77.   Love MI, Huber W, Anders S. Moderated estimation of fold change and dispersion for RNA-seq data with DESeq2. Genome Biol. 2014;15(12):550.